Geometry dependent Reduced-Order Models for the computation of homogenized transfer properties in porous Media

Antoine Moreau, Antoine Falaize, Cyrille Allery, Olivier Millet

(will be inserted by the editor)

Geometry dependent Reduced-Order Models for the computation of homogenized transfer properties in porous Media

Antoine Moreau · Antoine Falaize · Cyrille Allery · Olivier Millet

Received: April 15th, 2020 / Accepted: August 11th, 2021

Abstract This article investigates Reduced Order Models (ROMs) based on Proper Orthogonal Decomposition (POD) for efficient computation of the homogenized diffusion properties of saturated porous media. The homogenized tensor, whose classical expression may be obtained from periodic homogenization techniques, is computed by solving a local problem on an elementary cell that includes one or several circular solid inclusions. The cost of the repeated resolution of this problem by the Finite Element Method (FEM) for different inclusions radii may be important, and classical model order reduction methods based on the computation of a spatial basis can not be applied directly. The method proposed in this work to cope with the variability of circular inclusions relies on the introduction of a transformation from a reference domain to the physical domain that admits an exact affine decomposition in the three dimensional cases, allowing to split the problem into an offline learning phase and an online evaluation phase which does not depend on the number of degrees of freedom of the original full order solution. Approximate affine decomposition for two dimensional cases is also provided with an explicit estimation of the truncation error. The efficiency of the proposed algorithm in terms of accuracy and of computing time is evaluated firstly for 2D and 3D isotropic and anisotropic elementary cells with a single inclusion, and secondly for a 2D anisotropic cell with multiple inclusions. Furthermore the ROM is used to estimate in quasi-real time the homogenized diffusion tensor for a given probability distribution of the geometry parameters.

Keywords: Homogenization, Reduced Order Model, Proper Orthogonal Decomposition

1 Introduction

Diffusion in cementitious media is of crucial importance to estimate durability of reinforced concrete, as chlorides migrate across the pore solution, leading to rebar corrosion. Electrical double layer effects may occur when the Debye length (at the scale of nanometer for cementitious materials) is of the order of the pore size, resulting in a modification of transfer properties of ionic species. Ionic diffusion in saturated porous media is generally described by Nernst-Planck-Poisson system (NPP) or the Nernst-Planck-Poisson-Boltzmann system (NPPB) at the microscopic pore scale (the interested reader can refer to references [18, 20] for details). In order to estimate the lifetime of concrete structures, engineers must have at their disposal homogenized transfer models describing the diffusion at the material macroscale. Such models may be obtained by homogenization methods, whose best-known are periodic homogenization methods [5, 6, 32], volume averaging methods [2, 28, 29], or homogenization by two scale convergence [2, 19, 21, 22]. In the present work, we focus on the systems of equations obtained by periodic homogenization method, where the porous media microstructure is modelled as the periodic repetition of an elementary cell. Note that this approach has been also used in other physical contexts like advection or convection [4] and moisture diffusion [25].

The homogenization of NPP and NPPB systems to describe ionic diffusion in porous media has been performed in [8–11, 13, 26]. To determine the associated homogenized transfer properties at the macroscale (namely the homogenized diffusion tensor), we need to solve a partial differential equation (local problem) defined on an elementary cell characterizing the porous medium. Regarding cementicious media, such elementary cells may be modelled by a fluid phase across which

A. Moreau
E-mail: antoine.moreau@univ-lr.fr

A. Falaize
E-mail: antoine.falaize@univ-lr.fr

C. Allery
E-mail: cyrille.allery@univ-lr.fr

O. Millet
E-mail: olivier.millet@univ-lr.fr
LaSIE UMR-7356-CNRS, Université de La Rochelle Pôle Science et Technologie, Avenue Michel Crépeau 17042 La Rochelle Cedex 1, France

ions can migrate, with one or several ball shaped solid inclusions parametrized by their radii. The aim of this work is to propose a model order reduction procedure to evaluate, with reduced computational resources, the homogenized transfer properties of a porous medium when the geometry of its microstructure varies. The proposed approach consists in the construction of a reduced order model that takes into account the variability of the microstructure, thus avoiding the full numerical computation for each new geometry.

In the present work, the Reduced-Order Model (ROM) is constructed based on the Proper Orthogonal Decomposition (POD) [24,33]. This allows to approximate the solutions in a lower dimensional subspace that retains mean features of the original system. The POD-ROM approach has been widely used in Fluid mechanics [3,35], control problems [7] and solid mechanics [16]. In the scope of homogenization, the POD was already used to solve wave propagation in inhomogeneous media and Richards equation in an unsaturated soil [1], the non-linear homogenization of hyperelastic media at finite strains [36], hyperelastic heterogeneous structures [37], and has been combined with spectral decomposition in [17,23]. In these applications, the POD is applied to approximate the solutions parametrized by the time or the static loading while the geometry of the problem is fixed. In the present work, the parameter of interest is the geometry of the computational (fluid) domain so that the POD can not be applied directly since each solution belongs to a different functional space.

To overcome this difficulty, we propose a POD-ROM method based on a geometrical transformation that maps the fluid domain to a virtual reference fluid domain. The use of a mapping between the physical domain and a reference domain has been considered in previous works [30,31] in conjunction with the reduced basis method for geometries that can be well approximated by triangles, yielding to a reduced order model with an affine dependence to the geometry parameter. We propose in the present work a transformation specially tailored to address the circular geometries usually encountered in periodic homogenization of cementitious porous media. This transformation admits an exact affine decomposition in the three-dimensional cases, that allows a splitting of the classical operators associated with the homogenized NPPB problem. It yields as in [30,31] to a reduced order model with affine dependence to the geometry parameter, and without any reference to the number of degrees of freedom in the full order model. Approximate affine decomposition for two dimensional cases is also provided with an explicit estimation of the truncation error. Then, the computation of an orthogonal spatial basis of small size by POD method is straightforward, and a Galerkin projection of the physical problem onto this spatial POD basis results in a system of low order algebraic equations (ROM) whose resolution for a new geometry parameter is inexpensive. Furthermore, the resulting procedure could be used to build reduced order models for other kind of problems defined on geometries with circular or ball shaped components.

The paper is organized as follows. In section 2, the periodic homogenization of the multiscale ionic diffusion model is summarized and the classical cell problem is recalled. In section 3, the proposed POD based model order reduction method is presented. We firstly detail the procedure for an elementary cell with a single inclusion and secondly generalizes to the case of multiple inclusions. In section 4, we present numerical results that illustrate the accuracy and the reduced computational cost of the proposed method. Applications include isotropic and anisotropic elementary cells with single inclusion in 2D and 3D, a 2D anisotropic multi inclusions setting and the estimation in quasi-real time of the homogenized diffusion tensor for a given probability distribution of the geometry parameter.

2 Problem statement

In this section, we detail the motivations for the development of the model order reduction method proposed in section 3 for the computation of homogenized diffusion tensors parametrized by the geometry of the problem. First, we recall the Nernst-Planck-Poisson-Boltzmann (NPPB) equations that govern the ionic diffusion in porous media, taking into account the electrical double layer (EDL). Second, we state the nonlinear problem obtained from the classical periodic homogenization of the NPPB equations, along with the linear approximation applying in the usual cases for which the EDL can be neglected. Third, we recall the main steps in POD-based model order reduction and highlight the difficulties encountered with a direct application of this method to the linear problem due to the dependency to the geometry of the elementary cell .

2.1 Ionic diffusion in porous media

Here, we briefly recall the Nernst-Planck-Poisson-Boltzmann (NPPB) equations governing the ionic diffusion in porous media. The interested reader may refer to [15, 18, 20, 34] for more details. We denote by $\Omega \in \mathbb{R}^d$ the physical domain ($d \in \{2,3\}$) occupied by a saturated porous cementitious medium with path-wise connected fluid phase $\Omega_\mathrm{f} \subset \Omega$ through which ions can migrate, solid inclusions $\Omega_\mathrm{s} = \Omega \setminus \Omega_\mathrm{f}$ (not necessarily path-wise connected) and solid-fluid interface Γ (see figure 1).

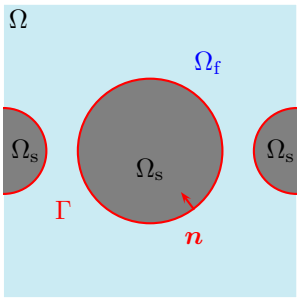

Fig. 1: Magnified view of a typical saturated porous medium, with fluid phase Ω_f, solid inclusions Ω_s and solid-fluid interface Γ.

The electro-diffusion in such media can be described by the Nernst-Planck equations governing the ionic diffusion coupled with the Poisson equation governing the electrical potential [14, 15, 34]. We consider the same simplifying assumptions as in [14, 15], *i.e.* there is no convection of the fluid in the pores and the ionic solution is in (1,1) cation-anion coordination. Then, denoting $c_\pm$ (mol.m^{-3}) the concentrations of anions and cations in the pore solution and ψ (V) the electrical potential, the Nernst-Planck equations read:

$$\frac{\partial c_\pm}{\partial t} - D_\pm \operatorname{div}\left(\nabla c_\pm + B\, c_\pm\, \nabla\psi\right) = 0, \quad \text{in } \Omega_\mathrm{f}, \tag{1}$$

$$\left(\nabla c_\pm + B\, c_\pm\, \nabla\psi\right)\cdot \boldsymbol{n} = 0, \quad \text{on } \Gamma, \tag{2}$$

where $D_\pm$ (m^2.s^{-1}) are the self-diffusion coefficients and $B = \frac{F}{RT}$ with T (K) the constant temperature, $F = 96485$ (Cb.mol^{-1}) the Faraday constant and $R = 8314$ (J.K.mol^{-1}) the perfect gas constant. The homogeneous Neumann boundary condition stands from the impermeability of the pores with $\boldsymbol{n}$ the unit normal vector on Γ exterior to Ω_f. The Poisson equation for the electrical potential reads:

$$\epsilon_v \Delta\psi + F\,(c_+ - c_-) = 0, \quad \text{in } \Omega_\mathrm{f}, \tag{3}$$

$$\epsilon_v \nabla\psi\cdot\boldsymbol{n} = \sigma, \quad \text{on } \Gamma, \tag{4}$$

where ϵ_v (C.V^{-1}.m^{-1}) is the electrical permittivity of the pore solution and σ (C.m^{-2}) is the surface charge density on Γ.

2.2 Periodic homogenization of ionic diffusion in porous media

Periodic homogenization is based on the assumption that the porous medium with characteristic length L (m) can be well approximated by the periodic repetition of a single microscopic cell with characteristic length ℓ (m), representative of the actual microstructure. Following the classical procedure of periodic homogenization, we introduce the coordinate systems $\boldsymbol{x}$ and $\boldsymbol{y}$ at the macroscopic scale and the microscopic scale, respectively, which are supposed to be independent. The electrical potential is decomposed as $\psi = \psi_\mathrm{b} + \varphi$ with ψ_b the bulk potential at the macroscopic scale and φ the Electrical Double Layer (EDL) potential at the microscopic scale [12, 14, 15]. The EDL is effective only in the vicinity of the boundary Γ so that it is assumed that $\varphi \simeq 0$ in the bulk sub-domain. Additionally, the ionic concentrations follow a Boltzmann distribution with $c_\pm = c_\mathrm{b}\, e^{\mp B\,\varphi}$ with c_b the bulk ionic concentration. Therefore, equations (3–4) rewrite as the so-called Poisson-Boltzmann equation at the microscopic scale:

$$\epsilon_v \Delta_{\boldsymbol{y}}\varphi - 2F\, c_\mathrm{b} \sinh\left(B\,\varphi\right) = 0, \quad \text{in } \Omega_\mathrm{f}, \tag{5}$$

$$\epsilon_v \nabla_{\boldsymbol{y}}\varphi\cdot\boldsymbol{n} = \sigma, \quad \text{on } \Gamma. \tag{6}$$

It is shown in [14, eq. (32-33)] that an asymptotic expansion of the solutions to NPPB equations at the leading order yields to a coupled diffusion-migration problem governing the ionic concentrations $c_\pm$ at the macroscopic scale and characterized by an homogenized diffusion tensor $\boldsymbol{D}_\pm$. In the remaining of the paper, we drop the distinction $\pm$ between anions and cations, focusing on the later without any loss of generality. The homogenized diffusion tensor is given by [14, 15]:

$$\boldsymbol{D} = \frac{1}{|\Omega|}\int_{\Omega_\mathrm{f}} D\, e^{-B\,\varphi}\,(\boldsymbol{I} + \nabla_{\boldsymbol{y}}\boldsymbol{\chi}^\intercal)\,\mathrm{d}\Omega, \tag{7}$$

where the vector-valued function $\boldsymbol{\chi} : \Omega_\mathrm{f} \to \mathbb{R}^d$ is the solution to the following local problem at the elementary cell scale:

$$\operatorname{div}_{\boldsymbol{y}}\left(D\, e^{-B\,\varphi}\,(\boldsymbol{I} + \nabla_{\boldsymbol{y}}\boldsymbol{\chi}^\intercal)\right) = 0 \quad \text{in } \Omega_\mathrm{f}, \tag{8}$$

$$\left(D\, e^{-B\,\varphi}\,(\boldsymbol{I} + \nabla_{\boldsymbol{y}}\boldsymbol{\chi})\right)\cdot\boldsymbol{n} = \boldsymbol{0} \quad \text{on } \Gamma, \tag{9}$$

where $\boldsymbol{I}$ denotes the identity matrix of appropriate dimension. Notice that the non-physical function $\boldsymbol{\chi}$ characterizes the geometry of the microstructure of the porous medium. When the characteristic length of the elementary cell is of several

orders larger than Debye length, the influence of the EDL can be neglected ($\varphi = 0$) so that the homogenized diffusion tensor is given by:

$$\boldsymbol{D} = \frac{1}{|\Omega|} \int_{\Omega_\mathrm{f}} D \, (\boldsymbol{I} + \nabla_{\boldsymbol{y}} \boldsymbol{\chi}^\intercal) \, \mathrm{d}\Omega, \tag{10}$$

with

$$\mathrm{div}_{\boldsymbol{y}} \, (\nabla_{\boldsymbol{y}} \boldsymbol{\chi}^\intercal) = 0, \quad \text{in } \Omega_\mathrm{f}, \tag{11}$$

$$(\boldsymbol{I} + \nabla_{\boldsymbol{y}} \boldsymbol{\chi}) \cdot \boldsymbol{n} = \boldsymbol{0}, \quad \text{on } \Gamma. \tag{12}$$

We focus on the computation of the homogenized diffusion tensor (10) which requires the resolution of the linear problem (11–12) for each geometry of the elementary cell, typically by the finite-element method. The purpose of the present work is to develop reduce-order modeling methods to circumvent this computational cost, taking into account the variability of the geometry.

2.3 Inapplicability of the classical POD based model order reduction

The Proper Orthogonal Decomposition (POD) is a method to derive empirical spatial modes (*i.e.* a spatial basis) from measurements or numerical data. Then, the so-called POD-based model order reduction aims at computing approximate solutions of the problems at hand that live in a subspace of the original solution space, usually by orthogonal projection. All the methods used to compute the POD basis rely on the solutions to an eigenvalue problem associated with a spatial correlation matrix which is formally defined as:

$$[\boldsymbol{C}]_{ij} = \int_\Omega \boldsymbol{u}(\boldsymbol{y}; \lambda_i) \cdot \boldsymbol{u}(\boldsymbol{y}; \lambda_j) \, \mathrm{d}\Omega, \tag{13}$$

where $\boldsymbol{u}(\boldsymbol{y}; \lambda_i)$ denotes the solution to the physical problem associated with a given parameter λ_i (usually the time or any physical property). In the present work, the construction of such a correlation matrix is not possible because all the solutions live in a functional space that is by definition parametrized by the shape of the spatial domain. Then, denoting ρ a geometry parameter, each solution $\boldsymbol{\chi}(\boldsymbol{y}; \rho)$ to the problem (11–12) lives in a functional space which is specific to the value of ρ, so that spatial correlations has no meaning in this context.

In this work, we address this issue by firstly mapping a reference domain to the physical domain through a transformation parametrized by the geometry, and secondly applying the POD-based model order reduction methodology in the reference domain to derive POD-ROMs that preserve the dependency to the actual geometry. As already stated in the introduction, the use of a mapping between the physical and a reference domain has been considered in previous works such as [30, 31] for geometries that can be well approximated by triangles, in conjunction with the reduced basis method. We detail in the next section the proposed POD-based model order reduction method specifically tailored to address the case of ball-shaped inclusions usually encountered in the context of periodic homogenization of porous media.

3 POD-ROM parametrized by the geometry of the elementary cell

We introduce below the proposed parametric POD-based reduced order model associated with the homogenized NPPB problem in order to evaluate efficiently the homogenized diffusion tensor $\boldsymbol{D}$ in equation (10) for a given geometry of the elementary cell. For the sake of clarity, we firstly consider a physical domain $\Omega = [-1, 1]^d$, $d = 2$, with a single solid inclusion $\Omega_\mathrm{s}(\rho) = \mathcal{B}(\boldsymbol{0}, \rho) \subset \mathbb{R}^d$ where $\mathcal{B}(\boldsymbol{y}_\mathrm{c}, \rho)$ denotes the d-dimensional ball of radius ρ centered at $\boldsymbol{y}_\mathrm{c}$. For this case, we define in subsection 3.1 the parametric transformation that maps a reference geometry to this actual elementary cell geometry. Then, we introduce in subsection 3.2 the proposed POD-based reduced-order model associated with the linear system (11-12) to compute the approximation $\widehat{\boldsymbol{\chi}} \simeq \boldsymbol{\chi}$ of the auxiliary function and the approximation $\widehat{\boldsymbol{D}} \simeq \boldsymbol{D}$ of the homogenized diffusion tensor. We secondly generalize the procedure to several inclusions associated with a vector of geometry parameters in subsection 3.3. Finally, we discuss the features of the proposed method. Notice that the presentation allows a direct generalization to the three-dimensional case considered in the next section devoted to numerical applications.

3.1 Mapping from a reference domain to the physical domain

The definition of the proposed parametric transformation that maps the reference domain $\Omega^\star = [-1, 1]^d$ to the actual elementary cell domain parametrized by the radius ρ of the solid inclusion is given below. Then, we detail some of its properties that will appear necessary in the construction of the POD-ROM. Finally, we make use of this transformation to state the variational problem associated with (10–12) posed on the reference domain.

3.1.1 Definition

The proposed transformation $\boldsymbol{\tau}_\rho : \Omega^\star \to \Omega$ is depicted in figure 2. It naturally divides the reference domain into three parts $\Omega^\star = \Omega^\star_\mathrm{s} \cup \Omega^\star_\mathrm{c} \cup \Omega^\star_\mathrm{e}$ where

$\Omega^\star_\mathrm{s} = \mathcal{B}(\mathbf{0}, \rho_\star)$ denotes the reference ball-shaped solid inclusion with constant reference radius $\rho_\star$,

$\Omega^\star_\mathrm{c} = \mathcal{B}(\mathbf{0}, q) \setminus \Omega^\star_\mathrm{s}$ denotes a crown around $\Omega^\star_\mathrm{s}$ of constant exterior radius q and interior radius $\rho_\star$,

$\Omega^\star_\mathrm{e} = \Omega^\star \setminus (\Omega^\star_\mathrm{s} \cup \Omega^\star_\mathrm{c})$ denotes the remaining domain exterior to $\Omega^\star_\mathrm{c}$.

The transformation $\boldsymbol{\tau}_\rho$ is defined as follows:

$$\boldsymbol{\tau}_\rho(\boldsymbol{\xi}) = \begin{cases} \alpha_\rho \boldsymbol{u}(\boldsymbol{\xi}) + \beta_\rho \boldsymbol{\xi}, & \text{if } \rho_\star \leq \| \boldsymbol{\xi} \| < q, \\ \boldsymbol{\xi}, & \text{if } \| \boldsymbol{\xi} \| \geq q, \end{cases} \tag{14}$$

where $\boldsymbol{u}(\boldsymbol{\xi}) = \dfrac{\boldsymbol{\xi}}{\| \boldsymbol{\xi} \|}$ denotes the radial unit vector and

$$\alpha_\rho = q\frac{\rho - \rho_\star}{q - \rho_\star}, \quad \beta_\rho = \frac{q - \rho}{q - \rho_\star}. \tag{15}$$

This transformation maps the reference fluid domain $\Omega^\star_\mathrm{f} = \Omega^\star_\mathrm{c} \cup \Omega^\star_\mathrm{e}$ to the physical fluid domain $\Omega_\mathrm{f}(\rho)$ and the reference solid-fluid interface is $\Gamma^\star$ to the physical interface $\Gamma(\rho)$, preserving barycenters (see figure 2).

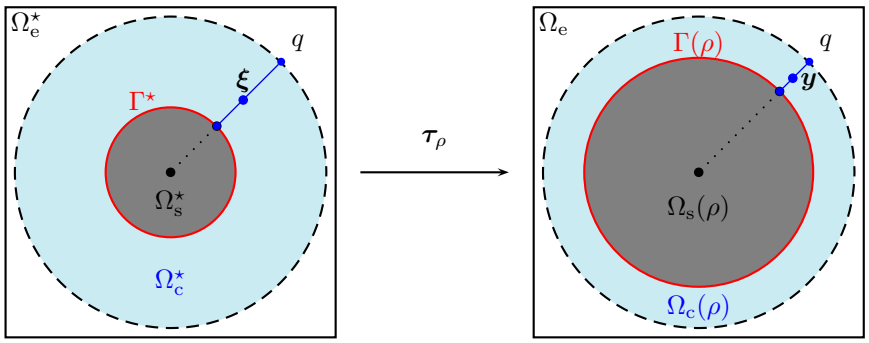

Fig. 2: Transformation $\boldsymbol{\tau}_\rho \colon \Omega^\star \overset{\boldsymbol{\xi} \mapsto \boldsymbol{\tau}_\rho(\boldsymbol{\xi}) = \boldsymbol{y}}{\longrightarrow} \Omega(\rho)$ defined in equation (14).

3.1.2 Properties

Any quantity of interest $a : \Omega \to \mathbb{R}^d$ defined over the physical domain can be expressed on the reference domain as $a(\boldsymbol{y}) = a\big(\boldsymbol{\tau}_\rho(\boldsymbol{\xi})\big) = a_\star(\boldsymbol{\xi})$ or equivalently $a_\star(\boldsymbol{\xi}) = a_\star\big(\boldsymbol{\tau}_\rho^{-1}(\boldsymbol{y})\big) = a(\boldsymbol{y})$. We have by the chain rule $\nabla_{\boldsymbol{y}} a(\boldsymbol{y}) = \nabla_{\boldsymbol{y}} a_\star\big(\boldsymbol{\tau}_\rho^{-1}(\boldsymbol{y})\big) = \nabla_{\boldsymbol{\xi}} a_\star(\boldsymbol{\xi}) \cdot \boldsymbol{J}_\rho^{-1}(\boldsymbol{\xi})$, where $\boldsymbol{J}_\rho(\boldsymbol{\xi}) = \nabla_{\boldsymbol{\xi}} \boldsymbol{\tau}_\rho(\boldsymbol{\xi})$ denotes the Jacobian matrix of the transformation. We also introduce $j_\rho(\boldsymbol{\xi}) = \det\big(\boldsymbol{J}_\rho(\boldsymbol{\xi})\big)$ the determinant of the Jacobian matrix and g_ρ the ratio of curvature of Γ to that of $\Gamma^\star$. Explicit formula for $\boldsymbol{J}_\rho^{-1}(\boldsymbol{\xi})$, $j_\rho(\boldsymbol{\xi})$ and g_ρ are given below (see appendix B for the proof):

$$\boldsymbol{J}_\rho^{-1}(\boldsymbol{\xi}) = \begin{cases} \dfrac{1}{\beta_\rho}\boldsymbol{I} - \dfrac{\alpha_\rho}{\beta_\rho} \cdot \dfrac{1}{\beta_\rho \|\boldsymbol{\xi}\| + \alpha_\rho} \boldsymbol{G}_{\boldsymbol{u}}(\boldsymbol{\xi}), & \text{if } \rho_\star \leq \|\boldsymbol{\xi}\| < q\ , \\ \boldsymbol{I}, & \text{if } q \leq \|\boldsymbol{\xi}\|, \end{cases} \tag{16}$$

where $\boldsymbol{G}_{\boldsymbol{u}}(\boldsymbol{\xi}) = \boldsymbol{I} - \dfrac{\boldsymbol{\xi} \cdot \boldsymbol{\xi}^\intercal}{\|\boldsymbol{\xi}\|^2}$,

$$j_\rho(\boldsymbol{\xi}) = \begin{cases} \displaystyle\sum_{p=0}^{d-1} \frac{C_{d-1}^p\, \alpha_\rho^p\, \beta_\rho^{d-p}}{\| \boldsymbol{\xi} \|^p}, & \text{if } \rho_\star \leq \|\boldsymbol{\xi}\| < q\ , \\ 1 & \text{if } q \leq \|\boldsymbol{\xi}\|. \end{cases} \tag{17}$$

where $C_{d-1}^p = \dfrac{(d-1)!}{p!(d-1-p)!}$ is the binomial coefficient and

$$g_\rho = \left(\frac{\rho}{\rho_\star}\right)^{d-1}. \tag{18}$$

3.1.3 Variational problem on the reference domain

We first state the variational formulation of the problem on the physical domain, and then uses the transformation (14) to formulate the variational problem on the reference domain. Since the problem (11–12) is defined up to an additive constant, it is necessary to introduce the following regularizing functional space of twice continuously differentiable L-periodic functions with zero spatial average over the fluide domain $\Omega_\mathrm{f}(\rho)$ with ρ the geometry parameter:

$$V_\rho = \left\{ u(\cdot;\rho) \in H^1_\sharp\big(\Omega_\mathrm{f}(\rho)\big);\ \int_{\Omega_\mathrm{f}(\rho)} u(\boldsymbol{y};\rho)\,\mathrm{d}\Omega(\rho) = 0 \right\}, \tag{19}$$

where $L = 2$ is the width of the square-shaped domain $\Omega_\mathrm{f}(\rho)$. Then, the variational formulation of the governing equations (11–12) is given for $\boldsymbol{\chi} \in \big(V_\rho\big)^d$ and $\forall \boldsymbol{v} \in \big(V_\rho\big)^d$ by

$$\int_{\Omega_\mathrm{f}(\rho)} \nabla_{\boldsymbol{y}} \boldsymbol{\chi} : \nabla_{\boldsymbol{y}} \boldsymbol{v}\,\mathrm{d}\Omega(\rho) = -\int_{\Gamma(\rho)} \boldsymbol{n}\cdot\boldsymbol{v}\,\mathrm{d}\Gamma(\rho). \tag{20}$$

Notice that the problem (20) above is suitable for a direct application of the finite-element method to obtain the solution for a single value of the geometry parameter ρ.

Making use of the Jacobian j_ρ of the transformation $\boldsymbol{\tau}_\rho$ proposed in section 3.1, we introduce the following functional space of twice continuously derivable L-periodic functions with zero spatial average over the reference fluid domain $\Omega^\star_\mathrm{f}$:

$$V_\star = \left\{ u_\star(\cdot;\rho) \in H^1_\sharp\big(\Omega^\star_\mathrm{f}\big);\ \int_{\Omega^\star_\mathrm{f}} u_\star(\boldsymbol{\xi};\rho)\, j_\rho\,\mathrm{d}\Omega^\star = 0 \right\}. \tag{21}$$

Then, the variational problem equivalent to (20) on the domain $\Omega^\star_\mathrm{f}$ reads for $\boldsymbol{\chi}_\star \in \big(V_\star\big)^d$ and $\forall \boldsymbol{v}_\star \in \big(V_\star\big)^d$:

$$\int_{\Omega^\star_\mathrm{c}} \left(\nabla_{\boldsymbol{\xi}}\boldsymbol{\chi}_\star \cdot \boldsymbol{J}_\rho^{-1}\right) : \left(\nabla_{\boldsymbol{\xi}}\boldsymbol{v}_\star \cdot \boldsymbol{J}_\rho^{-1}\right) j_\rho\,\mathrm{d}\Omega^\star + \int_{\Omega^\star_\mathrm{e}} (\nabla_{\boldsymbol{\xi}}\boldsymbol{\chi}_\star) : \nabla_{\boldsymbol{\xi}}\boldsymbol{v}_\star\,\mathrm{d}\Omega^\star = -\int_{\Gamma^\star} \boldsymbol{n}\cdot\boldsymbol{v}_\star\, g_\rho\,\mathrm{d}\Gamma^\star, \tag{22}$$

where $\boldsymbol{A} : \boldsymbol{B} = \mathrm{Tr}(\boldsymbol{A}\cdot\boldsymbol{B})$ with Tr the trace operator. Additionally, the homogenized diffusion tensor (10) is computed for a given auxiliary function $\boldsymbol{\chi}_\star$ defined over the reference domain as follows:

$$\boldsymbol{D}(\rho) = D\left(\frac{|\Omega^\star_\mathrm{f}|}{|\Omega^\star|}\boldsymbol{I} + \int_{\Omega^\star_\mathrm{c}} \left(\nabla_{\boldsymbol{\xi}}\boldsymbol{\chi}_\star \cdot \boldsymbol{J}_\rho^{-1}\right)^\intercal j_\rho\,\mathrm{d}\Omega^\star + \int_{\Omega^\star_\mathrm{e}} \nabla_{\boldsymbol{\xi}}\boldsymbol{\chi}_\star^\intercal\,\mathrm{d}\Omega^\star\right). \tag{23}$$

Note that $\left(\nabla_{\boldsymbol{\xi}}\boldsymbol{\chi}_\star \cdot \boldsymbol{J}_\rho^{-1}\right)^\intercal j_\rho = \left(\nabla_{\boldsymbol{\xi}}\boldsymbol{\chi}_\star \cdot \boldsymbol{J}_\rho^{-1} j_\rho\right)^\intercal$ and $\left(\nabla_{\boldsymbol{\xi}}\boldsymbol{\chi}_\star \cdot \boldsymbol{J}_\rho^{-1}\right) : \left(\nabla_{\boldsymbol{\xi}}\boldsymbol{v}_\star \cdot \boldsymbol{J}_\rho^{-1}\right) j_\rho = \left(\nabla_{\boldsymbol{\xi}}\boldsymbol{\chi}_\star \cdot \boldsymbol{J}_\rho^{-2} j_\rho\right) : \nabla_{\boldsymbol{\xi}}\boldsymbol{v}_\star$ due to the symmetry of operator $\boldsymbol{J}_\rho^{-1}$. Making use of these relations in (22–23) yields the following equivalent variational problem on the reference domain:

$$\int_{\Omega^\star_\mathrm{c}} \left(\nabla_{\boldsymbol{\xi}}\boldsymbol{\chi}_\star \cdot \boldsymbol{J}_\rho^{-2} j_\rho\right) : \nabla_{\boldsymbol{\xi}}\boldsymbol{v}_\star\,\mathrm{d}\Omega^\star + \int_{\Omega^\star_\mathrm{e}} (\nabla_{\boldsymbol{\xi}}\boldsymbol{\chi}_\star) : \nabla_{\boldsymbol{\xi}}\boldsymbol{v}_\star\,\mathrm{d}\Omega^\star = -\int_{\Gamma^\star} \boldsymbol{n}\cdot\boldsymbol{v}_\star\, g_\rho\,\mathrm{d}\Gamma^\star, \tag{24}$$

$$\boldsymbol{D}(\rho) = D\left(\frac{|\Omega^\star_\mathrm{f}|}{|\Omega^\star|}\boldsymbol{I} + \int_{\Omega^\star_\mathrm{c}} \left(\nabla_{\boldsymbol{\xi}}\boldsymbol{\chi}_\star \cdot \boldsymbol{J}_\rho^{-1} j_\rho\right)^\intercal \mathrm{d}\Omega^\star + \int_{\Omega^\star_\mathrm{e}} \nabla_{\boldsymbol{\xi}}\boldsymbol{\chi}_\star^\intercal\,\mathrm{d}\Omega^\star\right). \tag{25}$$

3.2 Geometry dependent POD-based Reduced-Order-Model

We introduce below the proposed POD-based reduced-order model to compute firstly the auxiliary function $\boldsymbol{\chi}$ and secondly the homogenized diffusion tensor $\boldsymbol{D}$. The efficiency of this construction relies on rewriting (24)–(25) as an affine combination of space-dependent quantities, with coefficients parametrized by the geometry parameters. This approach is usual in reduced-basis methods and is exposed, in the context of pulling back a parametrized to a reference domain, in [27], chapter 8. Thus, we first detail the requirements to derive such an affine dependency on the geometry parameters. We then show that these requirements are readily satisfied for three-dimensional geometries, and provide the construction of the associated POD-ROM. Then, we propose an approximate POD-ROM based on a truncated power series for two-dimensional geometries.

3.2.1 Affine dependency on the parameter

According to the previous subsection, the dependency on the geometry parameter in (24)–(25) is all contained in the terms $\boldsymbol{J}_\rho^{-k}\, j_\rho$, $k=1$ or 2. According to the binomial theorem, this expression can be formulated generically as follows:

$$\boldsymbol{J}_\rho^{-k}\, j_\rho = \frac{\beta_\rho^{1-k}}{\|\boldsymbol{\xi}\|^{d-1}} \sum_{\kappa=0}^{k} (-1)^\kappa \alpha_\rho^\kappa C_k^\kappa \left(\alpha_\rho + \beta_\rho \|\boldsymbol{\xi}\|\right)^{d-1-\kappa}. \tag{26}$$

Thus, a condition for an exact affine decomposition of (24–25) with respect to the geometry parameter ρ is that $d-1-\kappa \geq 0$. The worst case is $\kappa = 2$, so that the requirement on the dimension d reads:

$$d \geq 3. \tag{27}$$

3.2.2 Reduced-order model for three-dimensional geometries

Here, the requirement (27) is verified so that one can directly apply a Galerkin projection of the governing equation (24) for the auxiliary function, provided a suitable POD basis $\left(\boldsymbol{\phi}_i\right)_{1\leq i\leq n_{\boldsymbol{\chi}}}$ made of $n_{\boldsymbol{\chi}}$ spatial modes $\boldsymbol{\phi}_i \in \left(V_\star\right)^d$. This is done by firstly injecting in (24) the following ersatz:

$$\boldsymbol{\chi}_\star(\boldsymbol{\xi};\rho) \simeq \widehat{\boldsymbol{\chi}}_\star(\boldsymbol{\xi};\rho) = \sum_{j=1}^{n_{\boldsymbol{\chi}}} a_j(\rho)\, \boldsymbol{\phi}_j(\boldsymbol{\xi}), \tag{28}$$

then replacing successively the test-functions $\boldsymbol{v}_\star$ by the i-th mode $\boldsymbol{\phi}_i$, and finally injecting the relation (26) for $k=2$ and $d=3$. This results in the following reduced-order model:

$$\boldsymbol{A}_\rho \cdot \boldsymbol{a}(\rho) = \boldsymbol{c}_\rho, \tag{29}$$

for the coefficients $\boldsymbol{a}(\rho) = (a_1(\rho), \cdots, a_{n_{\boldsymbol{\chi}}}(\rho))$ of $\widehat{\boldsymbol{\chi}}_\star$ in the basis $\left(\boldsymbol{\phi}_i(\boldsymbol{\xi})\right)_{1\leq i\leq n_{\boldsymbol{\chi}}}$. Both sides of the POD-ROM equation (29) are given by:

$$\boldsymbol{A}_{\boldsymbol{\rho}} = \overline{\boldsymbol{A}} + \beta_\rho \widetilde{\boldsymbol{A}}_{0,0} + 2\alpha_\rho \widetilde{\boldsymbol{A}}_{1,0} + \frac{\alpha_\rho^2}{\beta_\rho}\widetilde{\boldsymbol{A}}_{2,0} - 2\alpha_\rho \widetilde{\boldsymbol{A}}_{-1,1} - \frac{\alpha_\rho^2}{\beta_\rho}\widetilde{\boldsymbol{A}}_{-2,1}, \tag{30}$$

and:

$$\boldsymbol{c}(\rho) = g_\rho\, \overline{\boldsymbol{c}}, \tag{31}$$

with

$$\left[\overline{\boldsymbol{A}}\right]_{ij} = \int_{\Omega_{\mathrm{e}}^\star} \nabla_{\boldsymbol{\xi}}\boldsymbol{\phi}_j : \nabla_{\boldsymbol{\xi}}\boldsymbol{\phi}_i \,\mathrm{d}\Omega^\star, \tag{32}$$

$$\left[\widetilde{\boldsymbol{A}}_{p,0}\right]_{ij} = \int_{\Omega_{\mathrm{c}}^\star} \frac{\nabla_{\boldsymbol{\xi}}\boldsymbol{\phi}_j : \nabla_{\boldsymbol{\xi}}\boldsymbol{\phi}_i}{\|\,\boldsymbol{\xi}\,\|^p} \,\mathrm{d}\Omega^\star, \text{ for } \; 0 \leq p \leq d-1, \tag{33}$$

$$\left[\widetilde{\boldsymbol{A}}_{r,1}\right]_{ij} = \int_{\Omega_{\mathrm{c}}^\star} \left(\nabla_{\boldsymbol{\xi}}\boldsymbol{\phi}_j \cdot \|\boldsymbol{\xi}\|^r \boldsymbol{G}_{\boldsymbol{u}(\boldsymbol{\xi})}\right) : \nabla_{\boldsymbol{\xi}}\boldsymbol{\phi}_i \,\mathrm{d}\Omega^\star, \text{ for } \; -2 \leq r \leq -1, \tag{34}$$

$$\left[\overline{\boldsymbol{c}}\right]_i = -\int_{\Gamma^\star} \boldsymbol{n}\cdot\boldsymbol{\phi}_i \,\mathrm{d}\Gamma^\star. \tag{35}$$

Injecting the ersatz (28) in equation (25) an making use of equation (26) yields the following low-cost evaluation of the homogenized diffusion tensor:

$$\boldsymbol{D}(\rho) \simeq \widehat{\boldsymbol{D}}(\rho) = D\left(\frac{|\Omega_{\mathrm{f}}^\star|}{|\Omega^\star|}\boldsymbol{I} + \boldsymbol{K}_\rho \cdot \boldsymbol{a}(\rho)\right), \tag{36}$$

with

$$\boldsymbol{K}_\rho = \overline{\boldsymbol{K}} + \beta_\rho^2 \widetilde{\boldsymbol{K}}_{0,0} + 2\alpha_\rho\beta_\rho \widetilde{\boldsymbol{K}}_{1,0} + \alpha_\rho^2 \widetilde{\boldsymbol{K}}_{2,0} - \alpha_\rho\beta_\rho\, \widetilde{\boldsymbol{K}}_{1,1} - \alpha_\rho^2\, \widetilde{\boldsymbol{K}}_{2,1}, \tag{37}$$

where:

$$\left[\overline{\boldsymbol{K}}\right]_{ijk} = \int_{\Omega_{\mathrm{e}}^\star} [\nabla_{\boldsymbol{\xi}}\boldsymbol{\phi}_k]_{ji} \,\mathrm{d}\Omega^\star, \tag{38}$$

$$\left[\widetilde{\boldsymbol{K}}_{p,0}\right]_{ijk} = \int_{\Omega_{\mathrm{c}}^\star} [\nabla_{\boldsymbol{\xi}}\boldsymbol{\phi}_k]_{ji} \frac{1}{\|\,\boldsymbol{\xi}\,\|^p} \,\mathrm{d}\Omega^\star, \text{ for } \; 0 \leq p \leq 2, \tag{39}$$

$$\left[\widetilde{\boldsymbol{K}}_{p,1}\right]_{ijk} = \int_{\Omega_{\mathrm{c}}^\star} [\nabla_{\boldsymbol{\xi}}\boldsymbol{\phi}_k \cdot \boldsymbol{G}_{\boldsymbol{u}(\boldsymbol{\xi})}]_{ji} \frac{1}{\|\,\boldsymbol{\xi}\,\|^p} \,\mathrm{d}\Omega^\star, \text{ for } \; 1 \leq p \leq 2. \tag{40}$$

3.2.3 Reduced-order model for two-dimensional geometries

The requirement (27) is not satisfied for $d = 2$, so that an exact affine decomposition of (24) is not possible. To cope with this difficulty, we express $\boldsymbol{J}_\rho^{-2}(\boldsymbol{\xi}) j_\rho$ as a convergent power series of $\|\boldsymbol{\xi}\|$ (see theorem 2 in appendix B), which can be truncated to yield the following approximation:

$$\boldsymbol{J}_\rho^{-2}\, j_\rho \simeq \left(1 + \frac{\alpha_\rho}{\beta_\rho \|\boldsymbol{\xi}\|}\right) \boldsymbol{I} - \left(1 + \beta_\rho^{n_\mathrm{t}+1} + (1-\beta_\rho)\left(\sum_{l=1}^{n_\mathrm{t}} (-1)^l \left(\sum_{m=l}^{n_\mathrm{t}} \beta_\rho^m C_m^l\right) \frac{\|\boldsymbol{\xi}\|^l}{q^l}\right)\right) \frac{\alpha_\rho}{\beta_\rho \|\boldsymbol{\xi}\|} \boldsymbol{G}_{\boldsymbol{u}(\boldsymbol{\xi})} \tag{41}$$

with $n_\mathrm{t} \geq 0$ the truncation order. The latter is chosen in practice as $n_\mathrm{t} = 2$ based on numerical experiments. The POD-based reduced-order model yields as follows:

$$\boldsymbol{A}_\rho \cdot \boldsymbol{a}(\rho) = \boldsymbol{c}_\rho, \tag{42}$$

for the coefficients $\boldsymbol{a}(\rho) = (a_1(\rho), \cdots, a_{n_{\boldsymbol{\chi}}}(\rho))$ of $\widehat{\boldsymbol{\chi}}_\star$ in the basis $\left(\boldsymbol{\phi}_i(\boldsymbol{\xi})\right)_{1 \leq i \leq n_{\boldsymbol{\chi}}}$. where both sides of the POD-ROM equation (29) are given by:

$$\boldsymbol{A}_{\boldsymbol{\rho}} = \overline{\boldsymbol{A}} + \left(\widetilde{\boldsymbol{A}}_{0,0} + \frac{\alpha_\rho}{\beta_\rho}\widetilde{\boldsymbol{A}}_{1,0}\right) - \left(1 + \beta_\rho^{n_\mathrm{t}+1}\right)\frac{\alpha_\rho}{\beta_\rho}\widetilde{\boldsymbol{A}}_{-1,1} + \sum_{l=1}^{n_\mathrm{t}} (-1)^l \left(\sum_{m=l}^{n_\mathrm{t}} \beta_\rho^m C_m^l\right)(1-\beta_\rho)\frac{\alpha_\rho}{\beta_\rho q^l}\widetilde{\boldsymbol{A}}_{l-1,1}. \tag{43}$$

The operator $\boldsymbol{J}_\rho^{-1}\, j_\rho$ in (25) is decomposed as in (26), providing exact formula for the reduced evaluation of the homogenized tensor $\boldsymbol{D}(\rho)$ in (36) with:

$$\boldsymbol{K}_\rho = \overline{\boldsymbol{K}} + \beta_\rho \widetilde{\boldsymbol{K}}_{0,0} + \alpha_\rho \widetilde{\boldsymbol{K}}_{1,0} - \alpha_\rho\, \widetilde{\boldsymbol{K}}_{1,1}. \tag{44}$$

3.3 Generalization to several inclusions

In this section we propose a direct generalization of the procedure described above to the case of several solid inclusions by firstly defining piecewise transformations over a set of subdomains centered on the inclusions and secondly assembling the reduced operators over this subdomains. Consider n_s non-overlapping ball-shaped solid inclusions $\Omega_{\mathrm{s},n}(\rho_n) = \mathcal{B}(\boldsymbol{y}_n, \rho_n)$, $1 \leq n \leq n_\mathrm{s}$, in the physical domain Ω, with the set of balls centers $\left\{\boldsymbol{y}_n\right\}_{1 \leq n \leq n_\mathrm{s}}$ and the vector of balls radii $\boldsymbol{\rho} = (\rho_n)_{1 \leq n \leq n_\mathrm{s}}$. The fluid phase is then $\Omega_\mathrm{f} = \Omega \setminus \left(\bigcup_{n=1}^{n_\mathrm{s}} \Omega_{\mathrm{s},n}(\rho_n)\right)$ with the solid-fluid interfaces $\Gamma_n(\rho_n)$, $1 \leq n \leq n_\mathrm{s}$ (see figure 3). We associate to this configuration the reference domain $\Omega^\star$ divided into the following subdomains:

- $\Omega^\star_{\mathrm{s},n} = \mathcal{B}(\boldsymbol{\xi}_n, \rho_\star)$ the reference solid inclusions centered at $\boldsymbol{\xi}_n = \boldsymbol{y}_n$ all with same reference radius $\rho_\star$,
- $\Omega^\star_{\mathrm{c},n} = \mathcal{B}(\boldsymbol{\xi}_n, q_n) \setminus \Omega^\star_{\mathrm{s},n}$ the crowns around the solid inclusions each with exterior radius q_n and interior radius $\rho_\star$,
- $\Omega^\star_\mathrm{e} = \Omega^\star \setminus \bigcup_{n=1}^{n_\mathrm{s}} (\Omega^\star_{\mathrm{s},n} \cup \Omega^\star_{\mathrm{c},n})$ the remaining fluid domain exterior to $\bigcup_{n=1}^{n_\mathrm{s}} \Omega^\star_{\mathrm{c},n}$.

Notice that we consider a single reference radius $\rho_\star$ to alleviate the notations and the generalization of the procedure described in this section to several reference radii is straightforward. Similarly to the case of a single inclusion, the transformation from the reference domain to the physical domain acts only on the crowns around the solid inclusions, which are required to be non-overlapping (see figure 3). It is defined as follows:

$$\boldsymbol{\tau}_{\boldsymbol{\rho}}(\boldsymbol{\xi}) = \begin{cases} \alpha_{\rho_n} \boldsymbol{u}(\boldsymbol{\xi} - \boldsymbol{\xi}_n) + \beta_{\rho_n}(\boldsymbol{\xi} - \boldsymbol{\xi}_n), & \text{if } \boldsymbol{\xi} \in \Omega^\star_{\mathrm{c},n}, \text{ for } 1 \leq n \leq n_\mathrm{s}, \\ \boldsymbol{\xi}, & \text{if } \boldsymbol{\xi} \in \overline{\Omega^\star_\mathrm{e}}, \end{cases} \tag{45}$$

where

$$\alpha_{\rho_n} = q_n \frac{\rho_n - \rho_\star}{q_n - \rho_\star}, \quad \beta_{\rho_n} = \frac{q_n - \rho_n}{q_n - \rho_\star}. \tag{46}$$

The computation of the Jacobian and the inverse Jacobian matrix for the transformation $\boldsymbol{\tau}_{\boldsymbol{\rho}}$ follows directly from the chain rule for the gradient of the radial unit vector which yields the following expressions:

$$\boldsymbol{J}_{\boldsymbol{\rho}}^{-1}(\boldsymbol{\xi}) = \begin{cases} \dfrac{1}{\beta_{\rho_n}}\left(\boldsymbol{I} - \alpha_{\rho_n} \dfrac{1}{\beta_{\rho_n}\|\boldsymbol{\xi} - \boldsymbol{\xi}_n\| + \alpha_{\rho_n}} \boldsymbol{G}_{\boldsymbol{u}(\boldsymbol{\xi} - \boldsymbol{\xi}_n)}\right), & \text{if } \boldsymbol{\xi} \in \Omega^\star_{\mathrm{c},n}, \text{ for } 1 \leq n \leq n_\mathrm{s}, \\ \boldsymbol{I}, & \text{if } \boldsymbol{\xi} \in \overline{\Omega^\star_\mathrm{e}}, \end{cases} \tag{47}$$

$$j_{\boldsymbol{\rho}}(\boldsymbol{\xi}) = \begin{cases} \displaystyle\sum_{p=0}^{d-1} \frac{C_{d-1}^p\, \alpha_{\rho_n}^p\, \beta_{\rho_n}^{d-p}}{\|\,\boldsymbol{\xi} - \boldsymbol{\xi}_n\,\|^p}, & \text{if } \boldsymbol{\xi} \in \Omega^\star_{\mathrm{c},n}, \text{ for } 1 \leq n \leq n_\mathrm{s}, \\ 1 & \text{if } \boldsymbol{\xi} \in \overline{\Omega^\star_\mathrm{e}}, \end{cases} \tag{48}$$

and the ratio of curvature of Γ_n to that of $\Gamma_n^\star$ is

$$g_{\rho,n} = \left(\frac{\rho_n}{\rho_\star}\right)^{d-1}, \; 1 \leq n \leq n_\mathrm{s}. \tag{49}$$

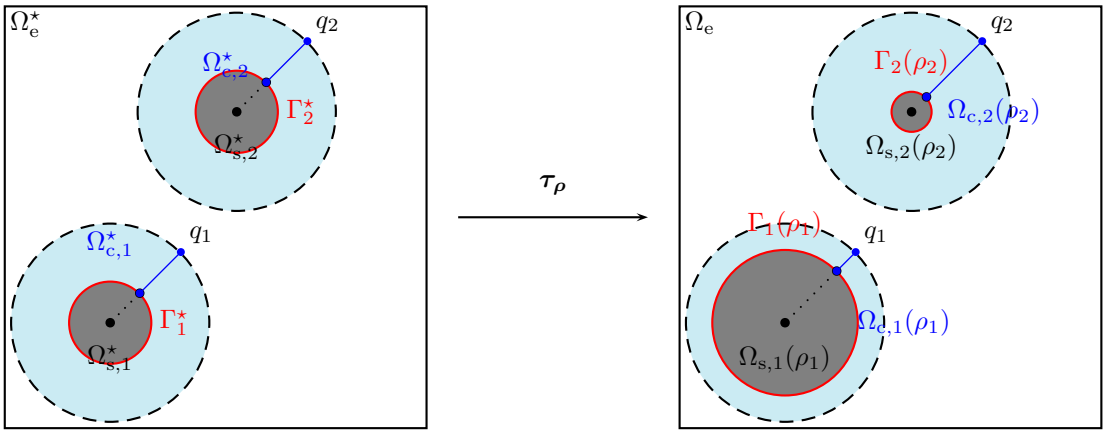

Fig. 3: Transformation $\boldsymbol{\tau_\rho}\colon \Omega^\star \overset{\boldsymbol{\xi}\mapsto\boldsymbol{\tau}_\rho(\boldsymbol{\xi})=\boldsymbol{y}}{\longrightarrow} \Omega(\rho)$ defined in equation (45) for $n_{\mathrm{s}}=2$ inclusions.

The variational problem associated with (11–12) for the multi-inclusions setting is given for $\boldsymbol{\chi} \in \left(V_\rho\right)^d$ and $\forall \boldsymbol{v} \in \left(V_\rho\right)^d$ by

$$\int_{\Omega_{\mathrm{f}}(\rho)} \nabla_{\boldsymbol{y}} \boldsymbol{\chi} : \nabla_{\boldsymbol{y}} \boldsymbol{v} \,\mathrm{d}\Omega = -\sum_{n=1}^{n_{\mathrm{s}}} \int_{\Gamma_n(\rho)} \boldsymbol{n}\cdot\boldsymbol{v}\,\mathrm{d}\Gamma(\rho), \tag{50}$$

with the same functional space V_ρ as for a single inclusion defined in (19), replacing the scalar parameter ρ by the vector parameter $\boldsymbol{\rho}$. Similarly, the variational problem on the reference domain $\Omega_{\mathrm{f}}^\star$ reads for $\boldsymbol{\chi}_\star \in \left(V_\star\right)^d$ and $\forall \boldsymbol{v}_\star \in \left(V_\star\right)^d$:

$$\sum_{n=1}^{n_{\mathrm{s}}} \int_{\Omega_{\mathrm{c},n}^\star} \left(\nabla_{\boldsymbol{\xi}}\boldsymbol{\chi}_\star \cdot \boldsymbol{J}_\rho^{-1}\right) : \left(\nabla_{\boldsymbol{\xi}}\boldsymbol{v}_\star \cdot \boldsymbol{J}_\rho^{-1}\right) j_\rho \,\mathrm{d}\Omega^\star + \int_{\Omega_{\mathrm{e}}^\star} \left(\nabla_{\boldsymbol{\xi}}\boldsymbol{\chi}_\star\right) : \nabla_{\boldsymbol{\xi}}\boldsymbol{v}_\star \,\mathrm{d}\Omega^\star = -\sum_{n=1}^{n_{\mathrm{s}}} \int_{\Gamma_n^\star} \boldsymbol{n}\cdot\boldsymbol{v}_\star\, g_{\rho,n}\,\mathrm{d}\Gamma^\star, \tag{51}$$

for the same functional space $V_\star$ defined in (21), replacing the scalar parameter ρ by the vector parameter $\boldsymbol{\rho}$. The homogenized diffusion tensor reads

$$\boldsymbol{D}(\boldsymbol{\rho}) = D\left(\frac{|\Omega_{\mathrm{f}}^\star|}{|\Omega^\star|}\boldsymbol{I} + \sum_{n=1}^{n_{\mathrm{s}}} \int_{\Omega_{\mathrm{c},n}^\star} \left(\nabla_{\boldsymbol{\xi}}\boldsymbol{\chi}_\star \cdot \boldsymbol{J}_{\boldsymbol{\rho}}^{-1}\right)^{\intercal} j_{\boldsymbol{\rho}}\,\mathrm{d}\Omega^\star + \int_{\Omega_{\mathrm{e}}^\star} \nabla_{\boldsymbol{\xi}}\boldsymbol{\chi}_\star^{\intercal}\,\mathrm{d}\Omega^\star\right). \tag{52}$$

The reduction is performed similarly to the single inclusion case with the same ersatz (28), resulting in the following reduced order models for the coefficients $\boldsymbol{a}(\boldsymbol{\rho}) = (a_1(\boldsymbol{\rho}), \cdots, a_{n_{\boldsymbol{\chi}}}(\boldsymbol{\rho}))$ of $\widehat{\boldsymbol{\chi}}_\star$ in the basis $\left(\boldsymbol{\phi}_i(\boldsymbol{\xi})\right)_{1\le i\le n_{\boldsymbol{\chi}}}$ in the two-dimensional case:

$$\boldsymbol{A}_{\boldsymbol{\rho}} \cdot \boldsymbol{a}(\boldsymbol{\rho}) = \boldsymbol{c}_{\boldsymbol{\rho}}, \tag{53}$$

with

$$\begin{aligned}\boldsymbol{A}_{\boldsymbol{\rho}} = \overline{\boldsymbol{A}} &+ \sum_{n=1}^{n_{\mathrm{s}}} \widetilde{\boldsymbol{A}}_{0,0,n} + \frac{\alpha_{\rho_n}}{\beta_{\rho_n}}\widetilde{\boldsymbol{A}}_{1,0,n} \\ &- \sum_{n=1}^{n_{\mathrm{s}}} \left(1+\beta_{\rho_n}^{n_{\mathrm{t}}+1}\right)\frac{\alpha_{\rho_n}}{\beta_{\rho_n}}\widetilde{\boldsymbol{A}}_{-1,1,n} \\ &+ \sum_{n=1}^{n_{\mathrm{s}}}\sum_{l=1}^{n_{\mathrm{t}}} (-1)^l \left(\sum_{m=l}^{n_{\mathrm{t}}} \beta_{\rho_n}^m C_m^l\right)(1-\beta_{\rho_n})\frac{\alpha_{\rho_n}}{\beta_{\rho_n} q^l}\widetilde{\boldsymbol{A}}_{l-1,1,n}\end{aligned} \tag{54}$$

and

$$\boldsymbol{c}(\rho) = \sum_{n=1}^{n_{\mathrm{s}}} g_{\rho,n}\,\overline{\boldsymbol{c}_n}, \tag{55}$$

where

$$\left[\overline{\boldsymbol{A}}\right]_{ij} = \int_{\Omega_{\mathrm{e}}^\star} \nabla_{\boldsymbol{\xi}}\boldsymbol{\phi}_j : \nabla_{\boldsymbol{\xi}}\boldsymbol{\phi}_i \,\mathrm{d}\Omega^\star, \tag{56}$$

$$\left[\widetilde{\boldsymbol{A}}_{p,0,n}\right]_{ij} = \int_{\Omega_{\mathrm{c},n}^\star} \frac{\nabla_{\boldsymbol{\xi}}\boldsymbol{\phi}_j : \nabla_{\boldsymbol{\xi}}\boldsymbol{\phi}_i}{\parallel \boldsymbol{\xi}-\boldsymbol{\xi}_n \parallel^p}\,\mathrm{d}\Omega^\star, \text{ for } \; 0\le p\le d-1, \tag{57}$$

$$\left[\widetilde{\boldsymbol{A}}_{r,1,n}\right]_{ij} = \int_{\Omega_{\mathrm{c},n}^\star} \left(\nabla_{\boldsymbol{\xi}}\boldsymbol{\phi}_j \cdot \|\boldsymbol{\xi}-\boldsymbol{\xi}_n\|^r \boldsymbol{G}_{\boldsymbol{u}(\boldsymbol{\xi}-\boldsymbol{\xi}_n)}\right) : \nabla_{\boldsymbol{\xi}}\boldsymbol{\phi}_i \,\mathrm{d}\Omega^\star, \text{ for } \; -1\le r\le n_{\mathrm{t}}-1, \tag{58}$$

$$\left[\overline{\boldsymbol{c}}_n\right]_i = -\int_{\Gamma_n^\star} \boldsymbol{n}\cdot\boldsymbol{\phi}_i \,\mathrm{d}\Gamma^\star. \tag{59}$$

The reduced order model for the homogenized diffusion tensor is given in the two-dimensional case by:

$$\boldsymbol{D}(\boldsymbol{\rho}) \simeq \widehat{\boldsymbol{D}}(\boldsymbol{\rho}) = D\left(\frac{|\Omega_{\mathrm{f}}^{\star}|}{|\Omega^{\star}|}\boldsymbol{I} + \boldsymbol{K}_{\boldsymbol{\rho}} \cdot \boldsymbol{a}(\boldsymbol{\rho})\right), \tag{60}$$

with

$$\boldsymbol{K}_{\rho} = \overline{\boldsymbol{K}} + \sum_{n=1}^{n_{\mathrm{s}}} \left(\beta_{\rho_n} \widetilde{\boldsymbol{K}}_{0,0,n} + \alpha_{\rho_n} \widetilde{\boldsymbol{K}}_{1,0,n} - \alpha_{\rho_n} \widetilde{\boldsymbol{K}}_{1,1,n}\right), \tag{61}$$

where

$$\left[\overline{\boldsymbol{K}}\right]_{ijk} = \int_{\Omega_{\mathrm{e}}^{\star}} [\nabla_{\boldsymbol{\xi}} \boldsymbol{\phi}_k(\boldsymbol{\xi})]_{ji} \, \mathrm{d}\Omega^{\star}, \tag{62}$$

$$\left[\widetilde{\boldsymbol{K}}_{p,0,n}\right]_{ijk} = \int_{\Omega_{\mathrm{c},n}^{\star}} \frac{[\nabla_{\boldsymbol{\xi}} \boldsymbol{\phi}_k(\boldsymbol{\xi})]_{ji}}{\| \boldsymbol{\xi} - \boldsymbol{\xi}_n \|^p} \, \mathrm{d}\Omega^{\star}, \tag{63}$$

$$\left[\widetilde{\boldsymbol{K}}_{p,1,n}\right]_{ijk} = -\int_{\Omega_{\mathrm{c},n}^{\star}} \frac{[\nabla_{\boldsymbol{\xi}} \boldsymbol{\phi}_k(\boldsymbol{\xi}) \cdot \nabla_{\boldsymbol{\xi}} \boldsymbol{u}(\boldsymbol{\xi} - \boldsymbol{\xi}_n)]_{ji}}{\| \boldsymbol{\xi} - \boldsymbol{\xi}_n \|^p} \, \mathrm{d}\Omega^{\star}. \tag{64}$$

Expressions for $\boldsymbol{A}_{\boldsymbol{\rho}}$ and $\boldsymbol{K}_{\rho}$ in the three-dimensional case are given by

$$\boldsymbol{A}_{\boldsymbol{\rho}} = \overline{\boldsymbol{A}} + \sum_{n=1}^{n_{\mathrm{s}}} \left(\beta_{\rho_n} \widetilde{\boldsymbol{A}}_{0,0,n} + 2\alpha_{\rho_n} \widetilde{\boldsymbol{A}}_{1,0,n} + \frac{\alpha_{\rho_n}^2}{\beta_{\rho_n}} \widetilde{\boldsymbol{A}}_{2,0,n} - 2\alpha_{\rho_n} \widetilde{\boldsymbol{A}}_{-1,1,n} - \frac{\alpha_{\rho_n}^2}{\beta_{\rho_n}} \widetilde{\boldsymbol{A}}_{-2,1,n}\right), \tag{65}$$

and

$$\boldsymbol{K}_{\rho} = \overline{\boldsymbol{K}} + \sum_{n=1}^{n_{\mathrm{s}}} \left(\beta_{\rho_n}^2 \widetilde{\boldsymbol{K}}_{0,0,n} + 2\alpha_{\rho_n}\beta_{\rho_n} \widetilde{\boldsymbol{K}}_{1,0,n} + \alpha_{\rho_n}^2 \widetilde{\boldsymbol{K}}_{2,0,n} - \alpha_{\rho_n}\beta_{\rho_n} \widetilde{\boldsymbol{K}}_{1,1,n} - \alpha_{\rho_n}^2 \widetilde{\boldsymbol{K}}_{2,1,n}\right). \tag{66}$$

Obviously, the procedure for a single inclusion is given by that for several inclusions with $n_{\mathrm{s}} = 1$, $\rho_1 = \rho$ and $\boldsymbol{y}_1 = 0$.

3.4 Discussion

The proposed method to compute the homogenized diffusion tensor splits into a training phase described in algorithm 1 and an evaluation phase described in algorithm 2. The training phase consists firstly in the computation of the auxiliary function by the finite-elements method for n_{ρ} sampling values of the geometry parameter, secondly in the computation of the POD basis and thirdly in the computation of the components of the reduced order model. The evaluation phase consists firstly in the assembly of reduced operators and secondly in the resolution of the reduced order model.

At the training phase, the computation of the auxiliary function in the reference domain can be done in two ways: (i) by solving the variational problem (50) for $\boldsymbol{\chi}(\boldsymbol{y}, \boldsymbol{\rho}_k)$ over the physical domain $\Omega_{\mathrm{f}}(\boldsymbol{\rho}_k)$ and transporting the solution to the reference domain $\Omega_{\mathrm{f}}^{\star}$, or (ii) by solving directly the variational problem (51). In both cases, it is required to solve n_{ρ} linear diffusion problems by the finite-elements method, and the first method requires n_{ρ} additional interpolations of the data onto a reference mesh, as illustrated in figure 4.

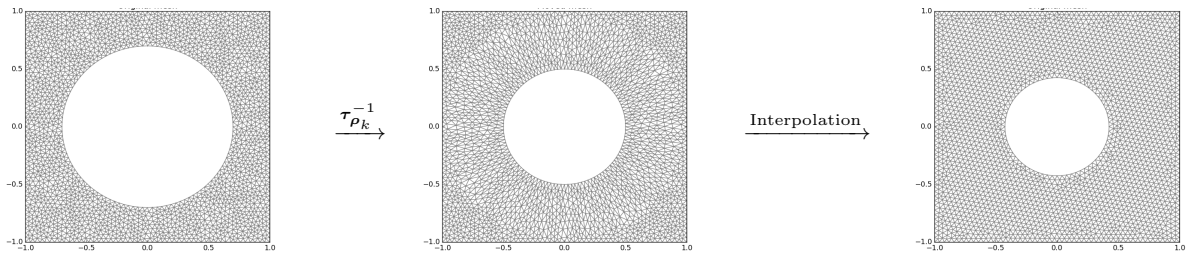

(a) Mesh on $\Omega_{\mathrm{f}}(\boldsymbol{\rho}_k)$ (b) Moved mesh on $\Omega_{\mathrm{f}}^{\star}$ (c) Reference mesh on $\Omega_{\mathrm{f}}^{\star}$

Fig. 4: Mesh used in the transport of the solution $\boldsymbol{\chi}(\boldsymbol{y}, \boldsymbol{\rho}_k)$ from the physical domain to the reference domain in step 2 of algorithm 1. The interpolation step is required to ensure that all the solutions $\{\boldsymbol{\chi}_{\star}(\boldsymbol{\xi}, \boldsymbol{\rho}_k)\}_{1 \leq k \leq n_{\rho}}$ in the reference domain are defined over the same mesh.

Algorithm 1: Offline phase to compute the elementary reduced tensors in (56–59) and (62–64).

Data: Set of geometry parameters $\{\boldsymbol{\rho}_k\}_{1\leq k\leq n_\rho}$.
Result: POD basis $(\boldsymbol{\phi}_i)_{1\leq i\leq n_{\boldsymbol{\chi}}}$ and reduced tensors in (56–59) and (62–64).
forall $k \leftarrow 1$ **to** n_ρ **do**
  Compute the auxiliary function $\boldsymbol{\chi}_\star(\boldsymbol{\xi},\boldsymbol{\rho}_k)$ either by (i) solving the variational problem (50) over the physical domain $\Omega_{\mathrm{f}}(\boldsymbol{\rho}_k)$ for $\boldsymbol{\chi}(\boldsymbol{y},\boldsymbol{\rho}_k)$ and transporting the solution to the reference domain $\Omega_{\mathrm{f}}^\star$ as in figure 4 or (ii) by solving directly the variational problem (51);
end
Assemble the matrix of snapshots $[\boldsymbol{S}]_{jk} = [\boldsymbol{\chi}_\star(\boldsymbol{\xi},\boldsymbol{\rho}_k)]_j$ for $1\leq j\leq n_{\mathrm{dof}}$ with n_{dof} the number of degrees of freedom of the finite elements space and $1\leq k\leq n_\rho$;
Compute the POD basis $(\boldsymbol{\phi}_i)_{1\leq i\leq n_{\boldsymbol{\chi}}}$ from the first $n_{\boldsymbol{\chi}}$ left singular vectors of $\boldsymbol{S}$;
Assemble the reduced tensors in (56–59) and (62–64);

Then the POD basis is computed using the Singular Value Decomposition (SVD) with asymptotic computational cost in $\mathcal{O}\left(n_{\mathrm{dof}}\, {n_{\boldsymbol{\chi}}}^2\right)$ with n_{dof} the number of degrees of freedom of the finite-elements space and $n_{\boldsymbol{\chi}}$ the truncation order associated with the number of POD modes. The computation of the components in (56–59) for the auxiliary function is done in $\mathcal{O}\big(((1+n_{\mathrm{s}}\,(3+n_{\mathrm{t}}))\,{n_{\boldsymbol{\chi}}}^2+n_{\mathrm{s}}\,n_{\boldsymbol{\chi}})\,n_{\mathrm{dof}}\big)$, respectively $\mathcal{O}\big(((1+5n_{\mathrm{s}})\,{n_{\boldsymbol{\chi}}}^2+n_{\mathrm{s}}\,n_{\boldsymbol{\chi}})\,n_{\mathrm{dof}}\big)$ operations, and the components in (62–64) for the homogenized tensor is done in $\mathcal{O}\big(4(1+3n_{\mathrm{s}})n_{\boldsymbol{\chi}}n_{\mathrm{dof}}\big)$, respectively $\mathcal{O}\big(9(1+5n_{\mathrm{s}})n_{\mathrm{dof}}\big)$ operations, for $d=2$ and $d=3$.
At the evaluation phase, it is required firstly to assemble the operator (54)–(55) in $\mathcal{O}\big((1+n_{\mathrm{s}}\,(3+n_{\mathrm{t}}))\,{n_{\boldsymbol{\chi}}}^2+n_{\mathrm{s}}\,n_{\boldsymbol{\chi}}\big)$ or $\mathcal{O}\big((1+5n_{\mathrm{s}})\,{n_{\boldsymbol{\chi}}}^2+n_{\mathrm{s}}\,n_{\boldsymbol{\chi}}\big)$ operations, and the operator (61) in $\mathcal{O}\big(4(1+3n_{\mathrm{s}})n_{\boldsymbol{\chi}}\big)$ or $\mathcal{O}\big(9(1+5n_{\mathrm{s}})n_{\boldsymbol{\chi}}\big)$ operations whether d is 2 or 3, and secondly to solve a linear system of size $n_{\boldsymbol{\chi}}$ in equation (53) and to perform d^2 direct contractions of vectors of size $n_{\boldsymbol{\chi}}$ in equation (60). Thus, the proposed method is particularly interesting when the number of degrees of freedom of the finite-elements space n_{dof} is very large (typically in the 3-dimensional cases) and when the homogenized diffusion tensor has to be evaluated for a large number of different geometry parameters. In practice, both offline and online computations can be further reduced by taking into account symmetries in tensors $\big[\boldsymbol{A}\big]_{ij}$ and $\boldsymbol{D}$.

Algorithm 2: Online phase to compute the POD-ROM approximations for the homogenized diffusion tensor $\widehat{\boldsymbol{D}}(\boldsymbol{\rho})$ and the auxiliary function $\widehat{\boldsymbol{\chi}}_\star(\boldsymbol{\xi};\boldsymbol{\rho})$ (optional).

Data: Target geometry parameter $\boldsymbol{\rho}$ and reduced tensors in (56–59) and (62–64) computed from algorithm 1.
Result: POD-ROM approximation for the homogenized diffusion tensor $\widehat{\boldsymbol{D}}(\boldsymbol{\rho})$ in (60) and (optional) the auxiliary function $\widehat{\boldsymbol{\chi}}_\star(\boldsymbol{\xi};\boldsymbol{\rho})$ in (28).
Assemble the matrix $\boldsymbol{A}_{\boldsymbol{\rho}}$ and the vector $\boldsymbol{c}_{\boldsymbol{\rho}}$ as in (54)–(55);
Solve the POD-ROM (53) for the coefficients $\boldsymbol{a}(\boldsymbol{\rho})$;
Assemble the matrix $\boldsymbol{K}_{\boldsymbol{\rho}}$ as in (61);
Compute the homogenized diffusion tensor $\widehat{\boldsymbol{D}}(\boldsymbol{\rho})$ from the POD-ROM (60);
(Optional) Assemble the POD-ROM approximation for the auxiliary function $\widehat{\boldsymbol{\chi}}_\star(\boldsymbol{\xi};\boldsymbol{\rho})$ as in (28);

4 Numerical results

In this section, we illustrate the accuracy and the reduced computational cost of the proposed method. We primarily focus on the ability of the method to approximate the homogenized diffusion tensor $\boldsymbol{D}$ in equation (10) when D is constant. However, since the latter splits in two terms as follows:

$$\boldsymbol{D} = \frac{D\,|\Omega_{\mathrm{f}}|}{|\Omega|}\boldsymbol{I} + \boldsymbol{T}, \qquad \boldsymbol{T} = \frac{D}{|\Omega|}\int_{\Omega_{\mathrm{f}}} \nabla_{\boldsymbol{y}}\boldsymbol{\chi}^{\intercal}\mathrm{d}\Omega, \tag{67}$$

and the computation of the the first part is easy for all geometries, we also focus on the computation of $\boldsymbol{T}$ which is more challenging. In the following, we compare the results obtained by solving the following numerical problems:

FOM corresponds to the classical full-order finite-element model associated with (50) defined over the physical domain which is remeshed for every value of the geometry parameter,

FOM$_\star$ corresponds to the full-order finite-element model associated with (51) define on a single reference domain for every value of the geometry parameter,

ROM denotes the reduced order model constructed from snapshots computed with the full order model labelled by FOM whose solutions are pulled back to the reference domain, distorting the mesh, and then interpolating on the reference mesh,

ROM$_\star$ denotes the reduced order model constructed from snapshots computed with the full order model labelled by FOM$_\star$ whose solutions are defined directly on the reference mesh.

As a first application, three different cell problems are considered in the case of a single solid inclusion:

(i) a two-dimensional isotropic cell, (ii) a three-dimensional isotropic cell and (iii) a three-dimensional anisotropic cell. As a second application, we consider a two-dimensional elementary cell with eight inclusions and two geometry parameters. Finally, we reconsider the previous applications when only a probability law is known for the geometry parameter.

All programs have been written in Python3 using packages from the FEniCS project, and executed on 4 CPU cadenced at 2.90GHz, with 16GB of working memory. In all this section, the full order solutions FOM and FOM$_\star$ are computed with quadratic Lagrange elements.

4.1 Single inclusion

For each case studied in this subsection, the test procedure is as follows. First, the influence of mesh refinement on the prediction of the tensor $\boldsymbol{T}$ defined in equation (67) obtained by solving the full-order problem FOM is tested. This step allows to select the mesh so that it does not influence the accuracy of the results of the POD-ROMs. Secondly, the efficiency of the proposed reduced order models ROM and ROM$_\star$ is evaluated. The accuracy will be studied by considering the relative error between the FOM and the POD-ROMs solutions, defined as:

$$e_{Dii} = \frac{D_{ii}^{\mathrm{ROM}} - D_{ii}^{\mathrm{FOM}}}{D_{ii}^{\mathrm{FOM}}}, \qquad e_{Tii} = \frac{T_{ii}^{\mathrm{ROM}} - T_{ii}^{\mathrm{FOM}}}{T_{ii}^{\mathrm{FOM}}}, \qquad e_{\boldsymbol{\chi}} = \frac{\|\boldsymbol{\chi} - \boldsymbol{\chi}^{\mathrm{FOM}}\|_{V_\star}}{\|\boldsymbol{\chi}^{\mathrm{FOM}}\|_{V_\star}}.$$

In the third case, the vector field $\boldsymbol{\chi}$ obtained from the resolution of FOM$_\star$, ROM or ROM$_\star$ over $\Omega_{\mathrm{f}}^\star$ is transported to Ω_{f} using transformation $\boldsymbol{\tau}_\rho$ and interpolated on the mesh for Ω_{f} in order to be compared with χ^{FOM}.

4.1.1 Single circular inclusion

The first microstructure is the periodical repetition of an elementary cell, which consists in a fluid domain with a solid inclusion forming a disc at the center (see figure 5). Due to the isotropy of this elementary cell, only computations of $D_{11}(\rho)$ and $T_{11}(\rho)$ are required.

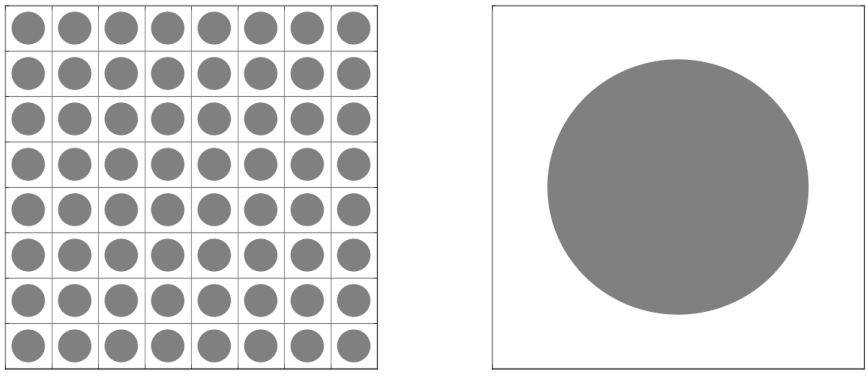

(a) Periodical microstructure (b) Elementary cell

Fig. 5: Two dimensional periodical microstructure and associated REV fluid domain with single solid circular inclusion parametrized by its radius ρ.

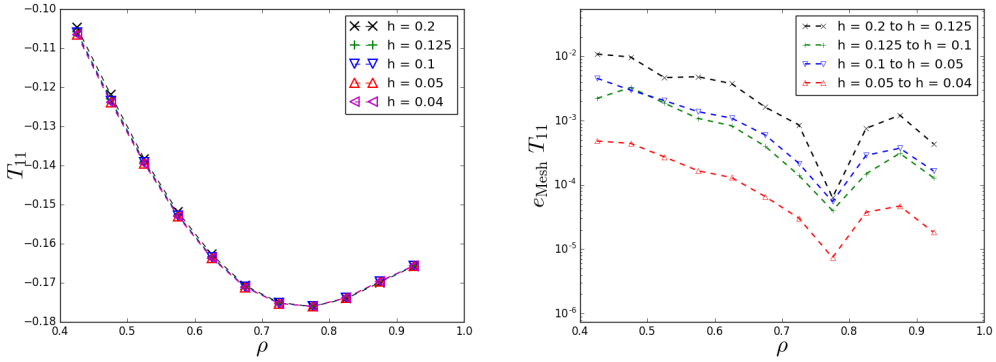

Fig. 6: Influence of the mesh for the prediction of T_{11} obtained by solving FOM.

a) Convergence of Finite Element Method with respect to the mesh size

Figures 6 show the influence of the mesh size on the computation of T_{11} obtained by solving the full-order model. On the right, the relative error of the component T_{11} given by:

$$e_{\text{Mesh},k} = \frac{T_{11}^{\text{Mesh}_{k+1}} - T_{11}^{\text{Mesh}_k}}{T_{11}^{\text{Mesh}_k}}, \tag{68}$$

obtained with two successive meshes is shown. We observe that the difference between two consecutive meshes is inferior to 0.1% as soon as $0.04 \leq h \leq 0.05$. Then, in the following, the snapshots required to build the POD basis are computed with a mesh size $h = 0.04$.

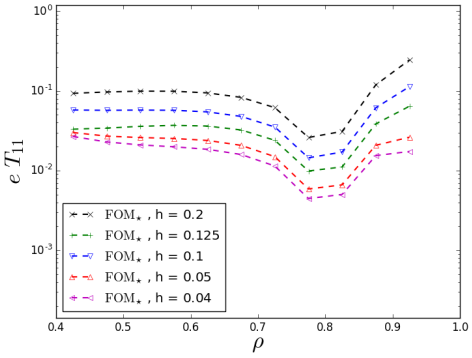

Fig. 7: Accuracy of the FOM$_\star$ to predict T_{11}. The error is defined as $\dfrac{T_{11}^{\text{FOM}_\star} - T_{11}^{\text{FOM},h=0.04}}{T_{11}^{\text{FOM},h=0.04}}$.

Figure 7 shows the ability of the FOM$_\star$ model to predict T_{11}, according to the mesh size. The reference corresponds to the solution obtained by FOM for a mesh size of $h = 0.04$. From $h = 0.05$ the error decrease is low. In the following we consider $h = 0.04$, that implies a maximal error of 3% between the predictions of FOM$_\star$ and FOM.

b) POD-ROM performances

The POD bases are built by considering 12 snapshots corresponding to values $\{0.4, 0.45, \ldots, 0.90, 0.95\}$ of radius ρ. For this range of radius, the volume fraction of the fluid phase varies between 0.29 and 0.87. The POD bases for ROM$_\star$ and ROM are truncated to 4 and 5 modes respectively, corresponding to an error of $\nu = 10^{-5}$ on the relative information content as given by formula (69) in appendix B. The transformation $\boldsymbol{\tau}_\rho$ is built with the reference radius $\rho_{\text{ref}} = 0.8$. The POD-ROMs are tested for the 11 values $\{0.425, 0.475, \ldots, 0.875, 0.925\}$ of $\tilde{\rho}$, which do not belong to the training set. D_{11}, T_{11} and $\boldsymbol{\chi}$ obtained with the full order models FOM, FOM$_\star$ and the POD-ROMs ROM, ROM$_\star$ are shown in figures 8 and 9.

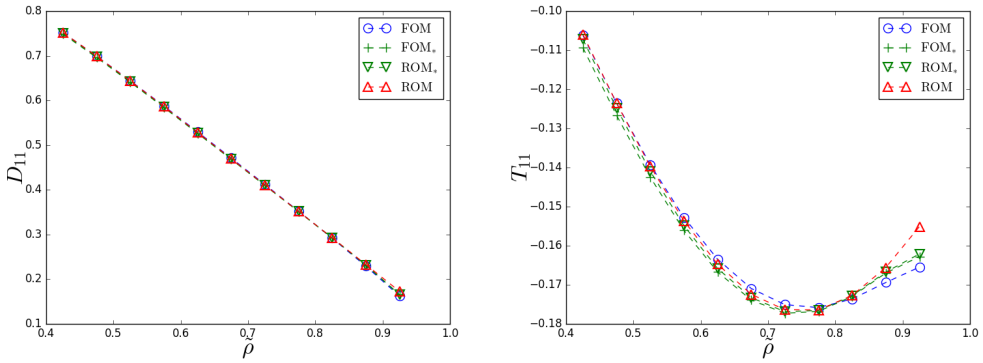

(a) Coefficient D_{11} (b) Coefficient T_{11}

Fig. 8: Comparison of D_{11} and T_{11} obtained by the full order models FOM, FOM$_\star$ and the reduced order models ROM, ROM$_\star$.

According to figure 8a, the diffusion coefficients D_{11} obtained with ROM, ROM$_\star$ and FOM$_\star$ are very close to those obtained by the reference FOM model. The same statement can be made for T_{11}, according to figure 8b, as far as the parameter $\tilde{\rho}$ is lesser than 0.825. For great values of the parameter, ROM$_\star$ results are close to those computed with FOM$_\star$, values of T_{11} obtained with ROM are slightly superior.

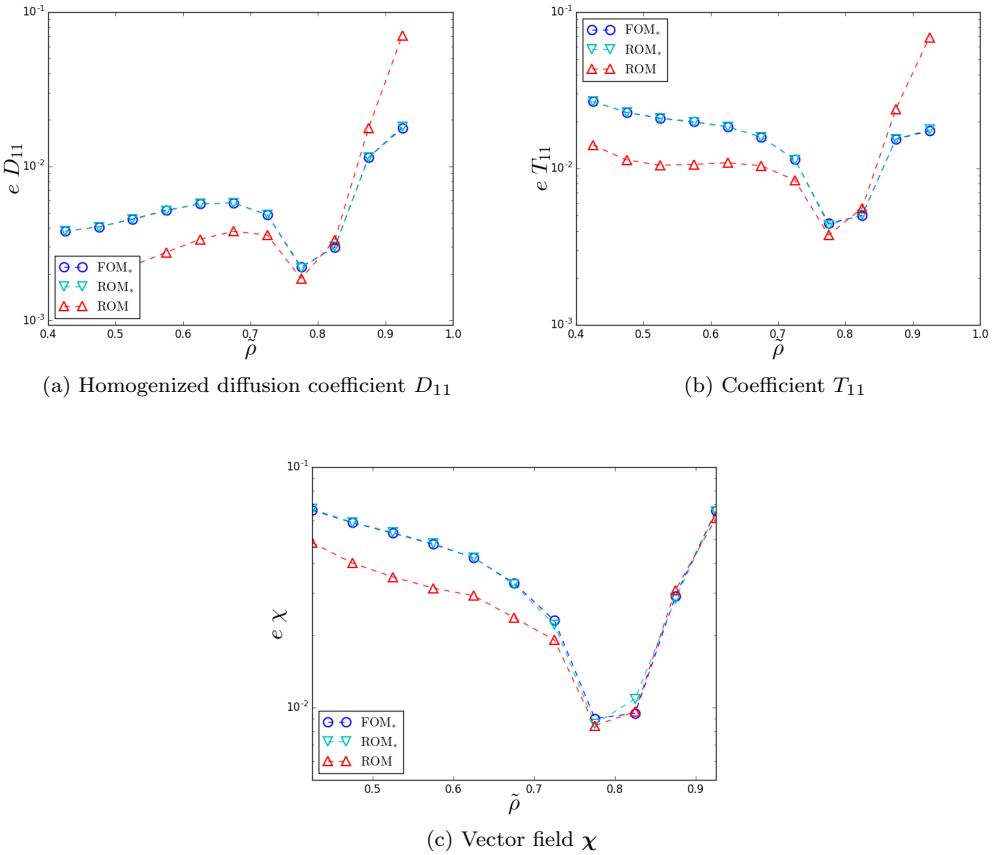

(a) Homogenized diffusion coefficient D_{11} (b) Coefficient T_{11}

(c) Vector field $\boldsymbol{\chi}$

Fig. 9: Errors associated with ROM, ROM$_\star$ and FOM$_\star$ on the prediction of D_{11}, T_{11} and $\boldsymbol{\chi}$ relatively to FOM.

Figures 9 show the relative errors between coefficients D_{11}, T_{11} and vector $\boldsymbol{\chi}$ predicted by the POD-ROMs and those obtained by the reference FOM. According to figure 9a, ROM$_\star$ is able to predict the coefficient D_{11}, with relative error smaller than 2%. The error for ROM is inferior to 8%, and even to 2% if $\tilde{\rho} \leq 0.9$. Moreover, both reduced-order models are able to predict coefficient T_{11} with a relative error lesser to 3%, when compared to FOM, except for $\tilde{\rho} \geq 0.9$ with ROM method where the error is lesser than 8% anyway. Furthermore, the relative error of vector $\boldsymbol{\chi}$ restituted by ROM$_\star$ and ROM is lesser than 6%. These errors are mainly due to the mapping onto the reference domain, or to

the use of the transformation Jacobian in the full-order problem on $\Omega^\star$. Indeed, the errors measured for ROM$_\star$ and FOM$_\star$ are the same, so that the POD-Galerkin projection is not involved. Moreover ROM gets errors that are slightly different from the ROM$_\star$'s, inferior to 3%.

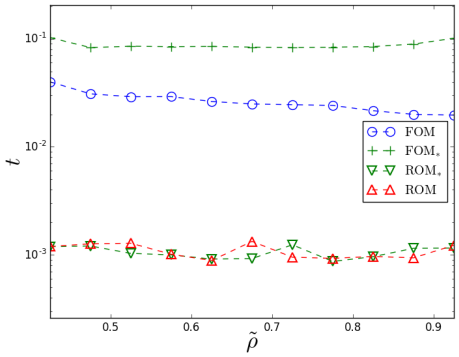

Fig. 10: Computing time for the full and reduced order models.

The online computing time is shown in figure 10. This figure exhibits efficiency of the POD-ROM. They allow to divide by 100 the computation time of $\boldsymbol{D}$ in comparison with the full simulation. We note also that the computing time of the full model FOM$_\star$ based on transformation $\boldsymbol{\tau}_\rho$ is greater than that of the standard full model FOM due to slower convergence of the underlying linear solver.

4.1.2 Single spherical inclusion

The second microstructure for which POD-ROM is performed to compute tensor $\boldsymbol{D}$ and $\boldsymbol{T}$ consists in the periodic repetition of a cubical cell with a single ball shaped solid inclusion located at the center of the cell (see figure 11). According to the symmetry of the elementary cell, the tensor $\boldsymbol{D}$ exhibits isotropic properties. Therefore, we limit the presentation of results to the tensor components D_{11} and T_{11}.

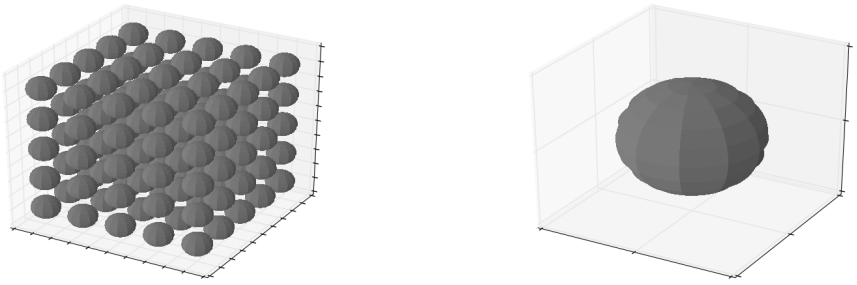

(a) Periodical microstructure (b) Elementary cell

Fig. 11: Three dimensional periodical microstructure and associated REV fluid domain with single solid spherical inclusion parametrized by its radius ρ.

a) Convergence of Finite Element Method with respect to the mesh size

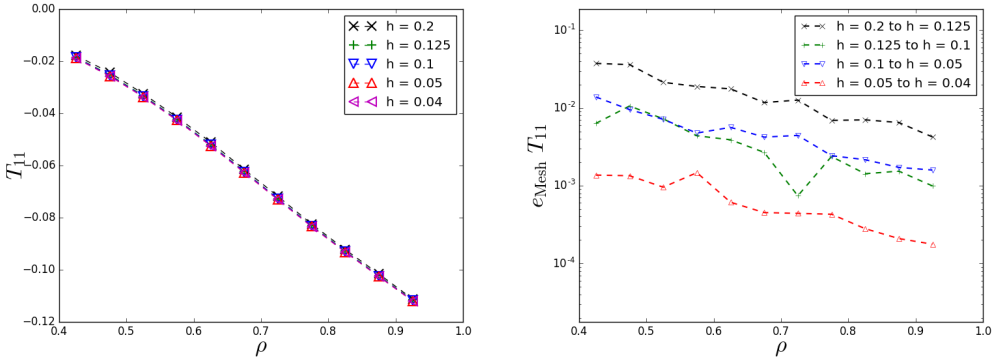

Fig. 12: Influence of the mesh for the prediction of T_{11} obtained by solving FOM.

The convergence of coefficient T_{11} with the mesh size and the associated relative error are shown in figure 12. Similarly to the previous 2D case, we see that relative errors between consecutive computations of T_{11} is low for $h \leq 0.05$ so we select $h = 0.05$ for this application.

b) POD-ROM performances

The POD bases are built by considering 12 snapshots corresponding to values $\{0.4, 0.45, \ldots, 0.90, 0.95\}$ of radius ρ. For this range of radius, the volume fraction varies between 0.55 and 0.97 for the fluid phase. Again, the POD bases for both ROM$_\star$ and ROM are truncated to 5 modes, corresponding to an error of $\nu = 10^{-5}$ on the relative information content as given by formula (69). The transformation $\boldsymbol{\tau}_\rho$ is built for $\rho_{\text{ref}} = 0.8$.

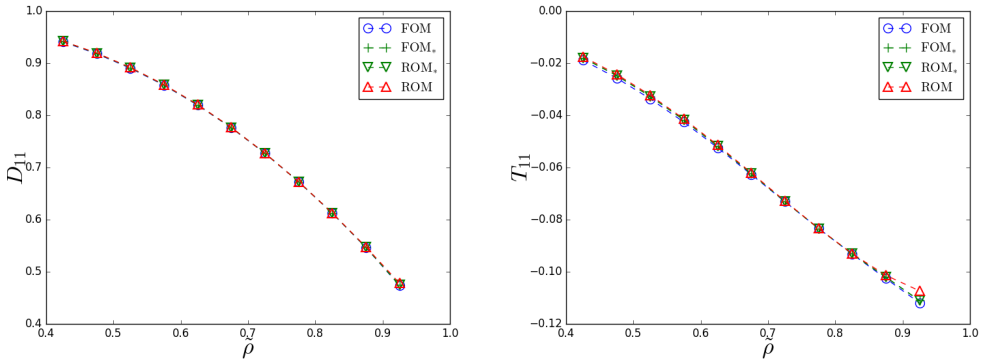

Fig. 13: D_{11} and T_{11} obtained by the full-order models and the reduced-order models.

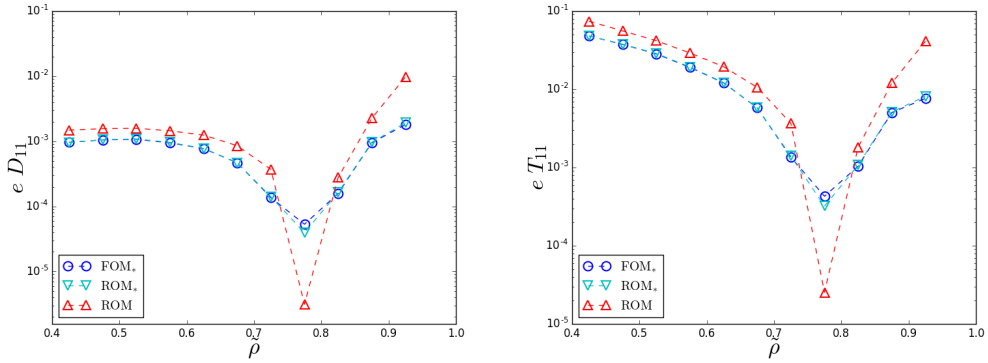

(a) Coefficient D_{11}

(b) Coefficient T_{11}

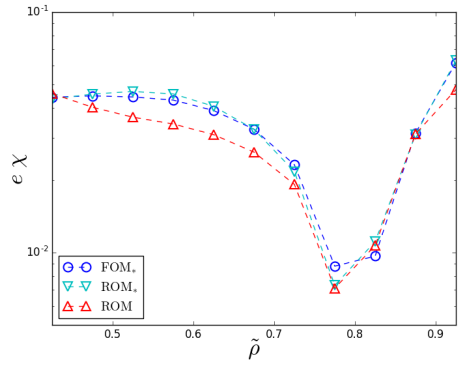

(c) Vector field $\boldsymbol{\chi}$

Fig. 14: Relative errors of ROM, ROM$_\star$ and FOM$_\star$ models relatively to FOM model, on the prediction of D_{11}, T_{11} and $\boldsymbol{\chi}$.

Figures 13 and 14 show that the POD-ROMs give a good prediction of the coefficient D_{11}. Indifferently from the offline POD-ROM construction, the relative error is below 1%. The latter error is below 8% for T_{11} and 6% for $\boldsymbol{\chi}$. Moreover, according to figure 15, ROM and ROM$_\star$ are 10000 times faster than FOM method. However, it should be noticed that the construction of the reduced order model ROM requires an additional interpolation step as detailed in algorithm 1.

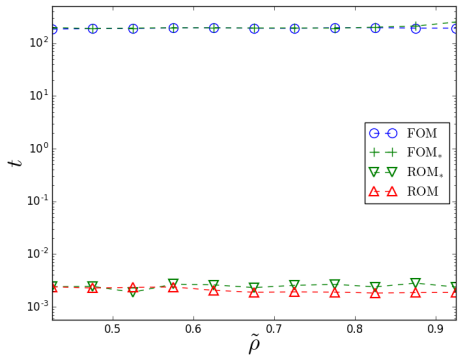

Fig. 15: Computing times for the full order models and reduced order models.

4.1.3 Three-dimensional anisotropic cell

The third microstructure studied in this article is defined by the anisotropic elementary cell in figure 16. Here, the tensor $\boldsymbol{T}$ is diagonal with coefficient T_{22} different of T_{11} and T_{33}, while the latter are identical. Indeed, axes represented in the right side of figure 16 indicate that axes Ox and Oz can be switched in a way that preserves the cell's geometry, while it is not the case if Oy is substituted to one of these two axes. In the following paragraph, results are presented for both T_{11} and T_{22}.

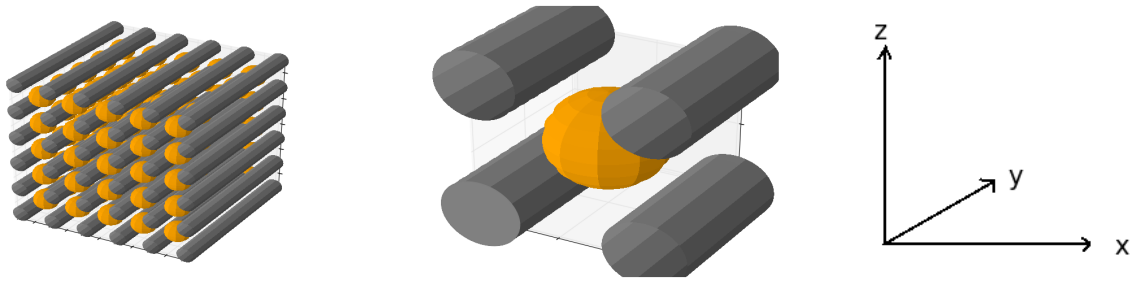

(a) Periodical microstructure (b) Elementary cell (c) Axes xyz

Fig. 16: Three dimensional periodic microstructure and associated REV fluid domain which includes one solid spherical inclusion parametrized by its radius ρ, and four quarters of cylinders independent from ρ located at the edges of the cell.

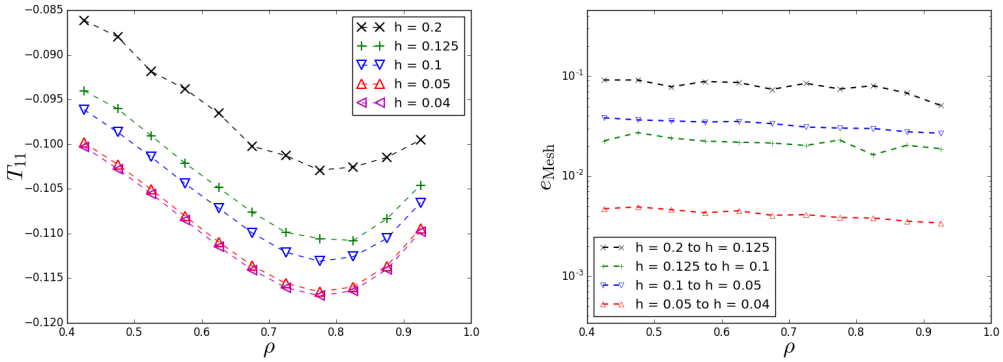

Fig. 17: Influence of the mesh for the prediction of T_{11} obtained by solving FOM.

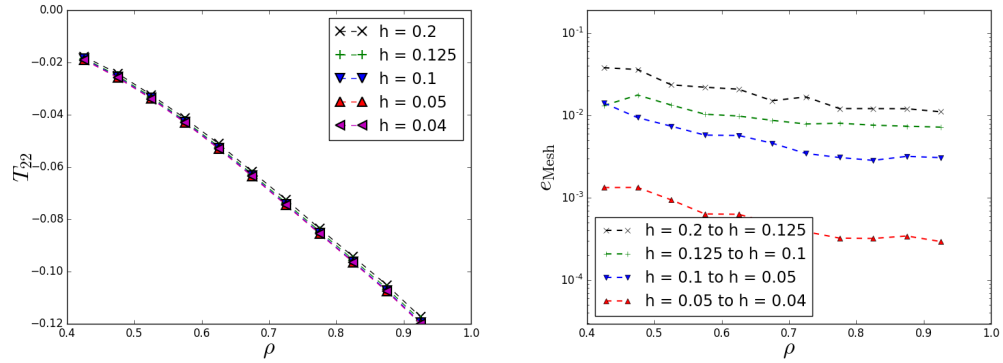

Fig. 18: Influence of the mesh for the prediction of T_{22} obtained by solving FOM.

a) Convergence of Finite Element Method with respect to the mesh size

The convergence of T_{11} and T_{22} with the mesh size and the associated relative error are shown in figure 17 and 18. We see that relative errors between consecutive computations of T_{11} and T_{22} is low for $h \leq 0.05$. Thus, we fix $h = 0.05$ for this application.

b) POD-ROM performances

The POD bases are built by considering 12 snapshots corresponding to values $\{0.4, 0.45, \ldots, 0.90, 0.95\}$ of radius ρ. For this range of radius, the volume fraction varies between 0.43 and 0.85 for the fluid phase. Again, the POD basis for ROM$_\star$ truncated to 6 modes and that for ROM is truncated to 5 modes, corresponding to an error of $\nu = 10^{-5}$ in (69). Transformation $\boldsymbol{\tau}_\rho$ is built with $\rho_{\text{ref}} = 0.8$. In this paragraph, results obtained with the different models are presented similarly to the previous example.

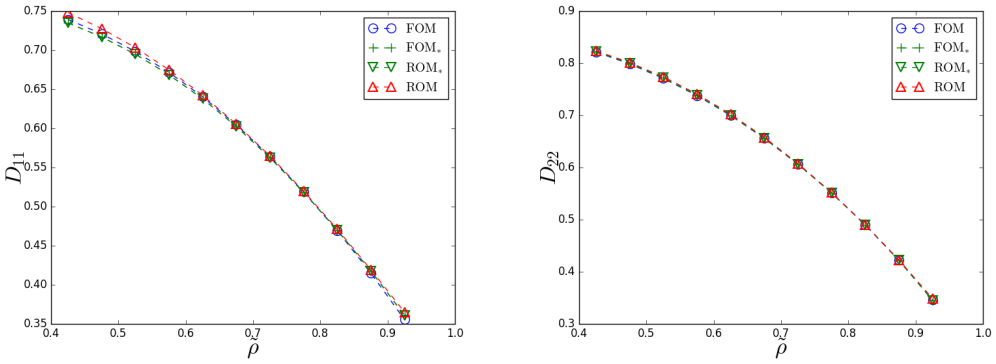

Fig. 19: D_{11} and D_{22} obtained by the full-order models and the reduced-order models.

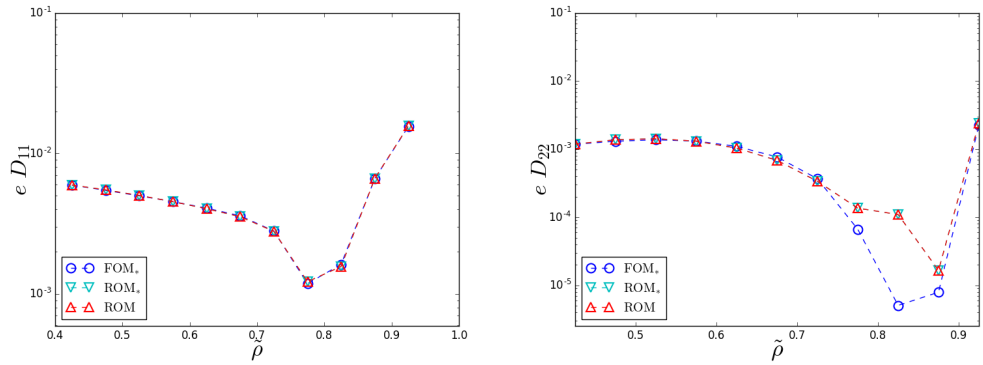

(a) Coefficient D_{11} (b) Coefficient D_{22}

Fig. 20: Relative errors of components D_{11} and D_{22} of the homogenized tensor, between the predictions of the reduced-order models and the reference full-order model FOM.

Figures 19 and 20 show that POD-ROM gives an accurate prediction of the diffusion coefficients D_{11} and D_{22}. The relative error with respect to FOM is inferior to 2% for D_{11} and 0.2% for D_{22}.

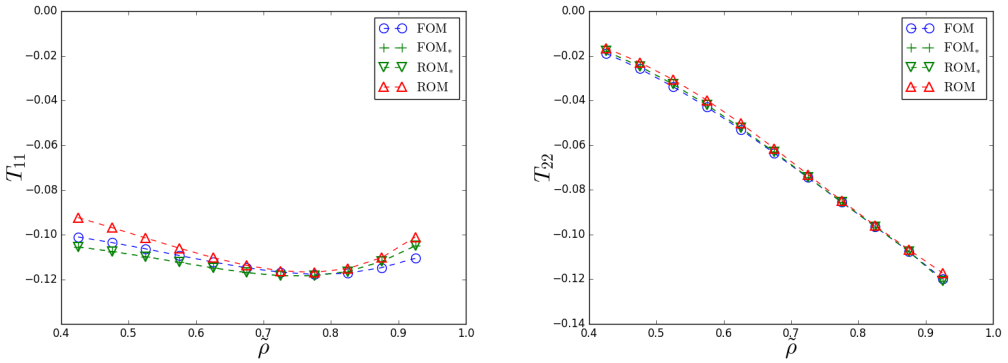

(a) T_{11} (b) T_{22}

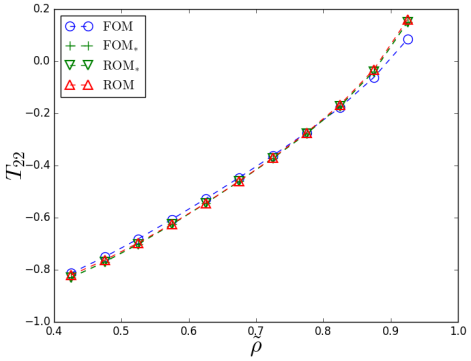

(c) $\frac{T_{22}-T_{11}}{T_{11}}$

Fig. 21: T_{11}, T_{22} and $\dfrac{T_{22}-T_{11}}{T_{11}}$ obtained by the POD-ROMs and Finite Element Method.

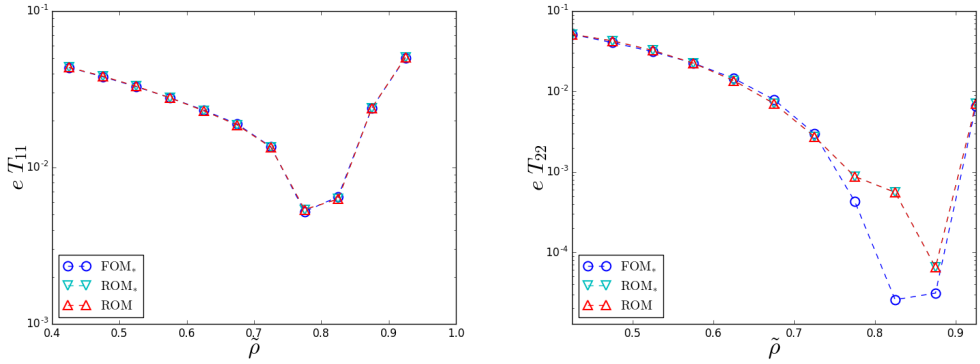

(a) Coefficient T_{11} (b) Coefficient T_{22}

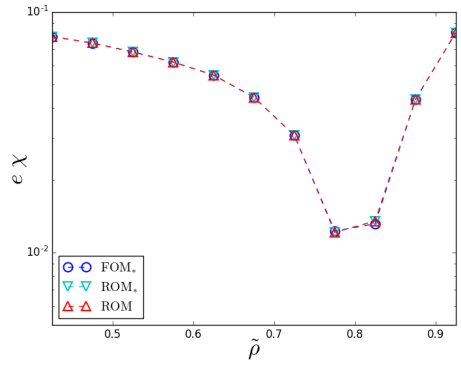

(c) Vector field $\boldsymbol{\chi}$

Fig. 22: Relative errors: vector field $\boldsymbol{\chi}$ and $\boldsymbol{T}$ coefficients.

Figures 21 and 22 confirm these results. ROM$_\star$and ROM allow to predict $\boldsymbol{T}$'s coefficients with lesser that 6% error in all cases, moreover $\boldsymbol{\chi}$ is restituted with less than 8% error. Furthermore, figure 21c shows that the cell's anisotropy is well restituted by POD-ROM. Figure 23 shows that POD-ROM, executed online, is 10000 times faster than FEM.

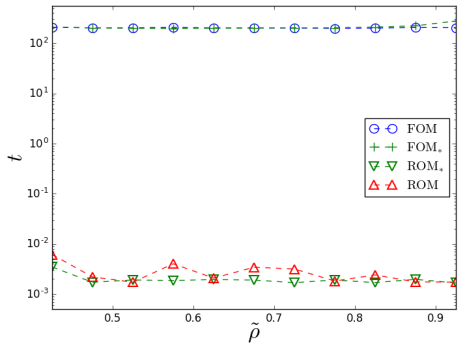

Fig. 23: Computing time for the full and reduced models

4.1.4 Random distributions of a scalar parameter

Here we are interested in the computation of the components of the homogenized tensor $\boldsymbol{D}(\rho)$ when only a probability law is known for ρ. For each of the three configurations addressed previously, a normal distribution $\mathcal{N}\left(m, \sigma^2\right)$ with $m = \rho_{\text{ref}}$ and $\sigma = 0.15$ is simulated by the Monte-Carlo method, providing a pseudo-random value of the parameter ρ for which $\boldsymbol{D}(\rho)$ is computed online with ROM.

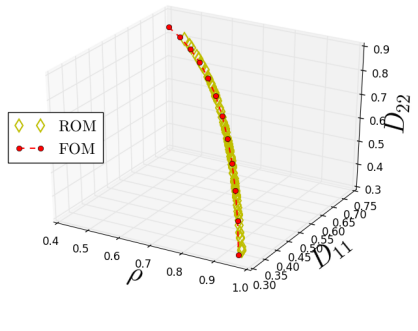

(a) One circular inclusion.

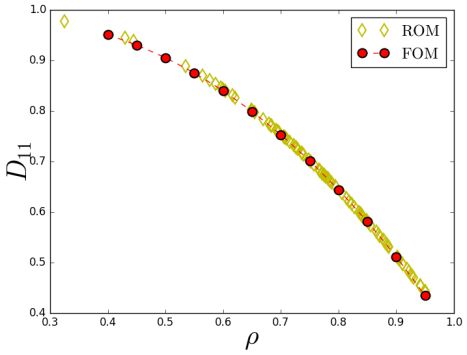

(b) One spherical inclusion.

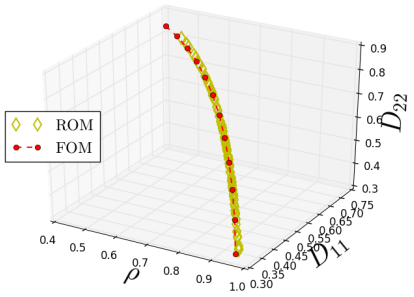

(c) 3D anisotropic cell.

Fig. 24: Distribution of $\boldsymbol{D}(\rho)$: 100 occurences of ρ and probability law $\mathcal{N}(0.80, 0.15)$ compared with 8 values obtained from the Finite Element Method.

On figure 24, it can be seen that the direct calculation of $D_{11}(\rho)$ (respectively $D_{11}(\rho)$) where ρ follows the probability law $\mathcal{N}(0.70, 0.15)$ (in yellow) interpolates with high accuracy the eight values $D_{11}(\rho^j)$ (respectively $D_{22}(\rho^j)$) computed with FOM (in red), where ρ^j belongs to the training set. Once the offline part of POD-ROM computation is performed, the distribution of $\boldsymbol{D}(\rho)$ can be estimated in real time for a given probability law simulated by Monte-Carlo.

4.2 Multiple inclusions with various parameters

We now focus on an elementary cell with 8 circular inclusions parametrized by two radii ρ_1 and ρ_2 (see figure 25a). The elementary cell $\Omega = (-1, 1)^2$ consists in a fluid phase and of eight solid discs whose centers have coordinates $(0, 35; 0)$, $(0; 0, 25)$, $(-0, 35; 0)$, $(0; -0, 25)$, $(0; 0, 75)$, $(0, 75; 0)$, $(0; -0, 75)$, $(-0, 75; 0)$. The radii $\rho_{\star 1}$ and $\rho_{\star 2}$ of the reference configuration are both set to $0, 1125$. Computations of T_{11} and T_{22} with FOM using different meshes lead us to choose the value $h = 0.02$ for the mesh resolution. Figure 25b shows the solution of the full-order cell problem.

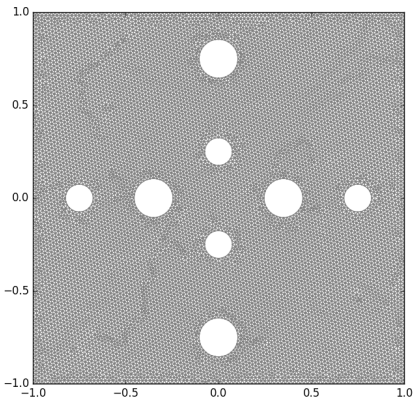

(a) Mesh, $h = 0.02$

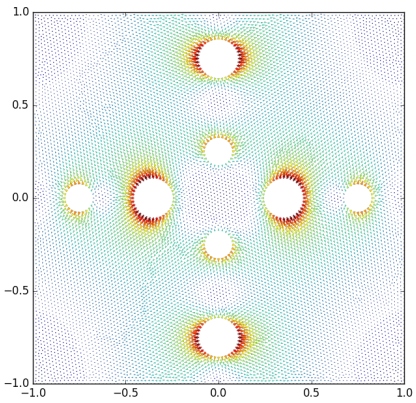

(b) $\boldsymbol{\chi}$ computed with FOM

Fig. 25: Mesh and FOM solution for the case: $(\rho_1, \rho_2) = (0.0975, 0.0675)$.

The POD bases are built by considering 36 snapshots corresponding to the six values $\{0,0525; 0.0675; \ldots; 0,1275; 0,1425\}$ taken independently by each parameter ρ_1, ρ_2. By choosing $\nu = 10^{-5}$, there are 7 modes for ROM$_\star$ and 34 modes for ROM. The reduced order models are tested for the 36 values of $(\tilde{\rho_1}, \tilde{\rho_2})$ where each parameter takes independently the 6 values $\{0,06; 0,075, \ldots; 0,135\}$ which do not belong to the training set.The choice of $(0.1125, 0.1125)$ for the reference values of parameters ρ_1 and ρ_2 is motivated, like in the monoparametric cases seen in this work, by the accuracy of ROM$_\star$ and ROM. For each couple (ρ_1, ρ_2), the logarithm of the relative error between the solutions obtained by ROM$_\star$ (respectively ROM) are shown in figure 26 (respectively figure 27). The ROM and ROM$_\star$ methods restitute T_{11} and T_{22} with less than 1% error for most of the 36 parameter pairs (ρ_1, ρ_2), in fact the error is lesser than 3% for each tested value and reachs 0.1% when (ρ_1, ρ_2) is close to $(\rho_{\star 1}, \rho_{\star 2})$. Furthermore, the vector field $\boldsymbol{\chi}$ is restituted by the ROM method with less than 10% error for each bi-parameter value, and this error reachs 1% in a vicinity of $(\rho_{\star 1}, \rho_{\star 2})$. Finally, the value of $\dfrac{T_{22} - T_{11}}{T_{11}}$, which quantifies the anisotropy, is shown in figure 28 for each of the 36 tested pairs (ρ_1, ρ_2). Both POD-ROMs reproduce properly this coefficient 100 times faster than FOM.

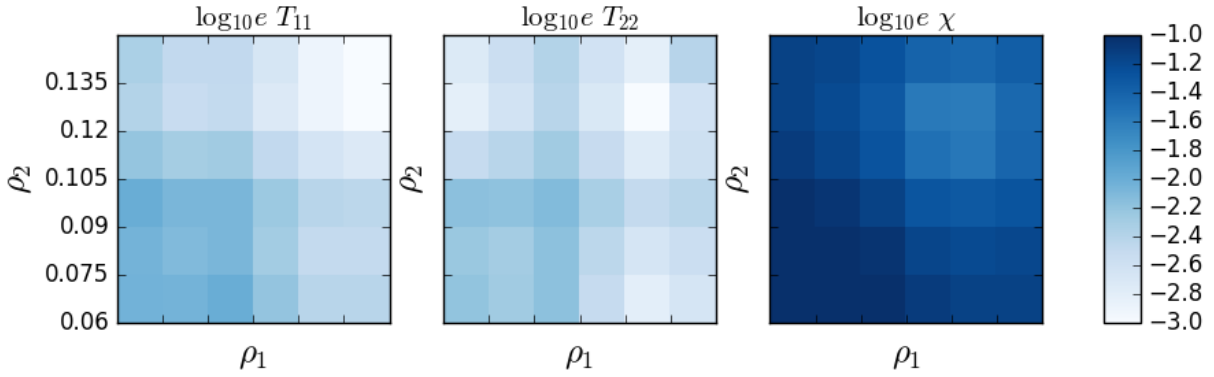

Fig. 26: Relative error of ROM$_\star$, relatively to FOM, on the prediction of coefficients T_{11}, T_{22} and of vector field $\boldsymbol{\chi}$. The value of ρ_2, which changes in the same range than ρ_2, is recalled at the left side of the first plot.

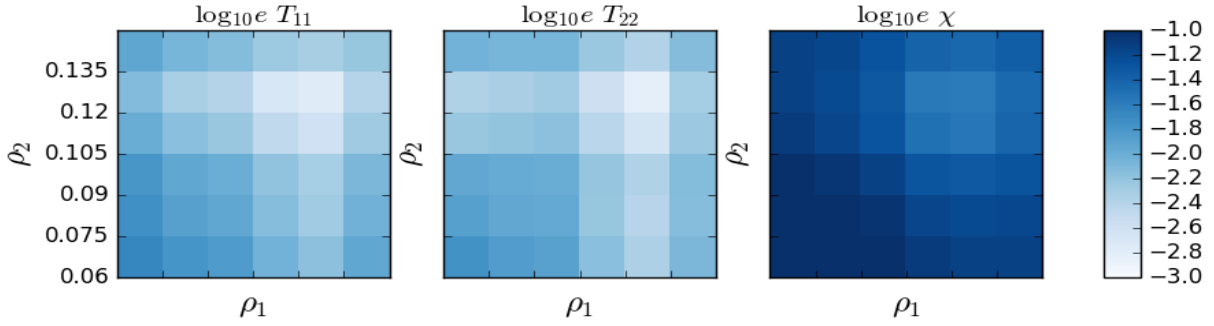

Fig. 27: Relative error of ROM, relatively to FOM, on the prediction of coefficients T_{11}, T_{22} and of vector field $\boldsymbol{\chi}$.

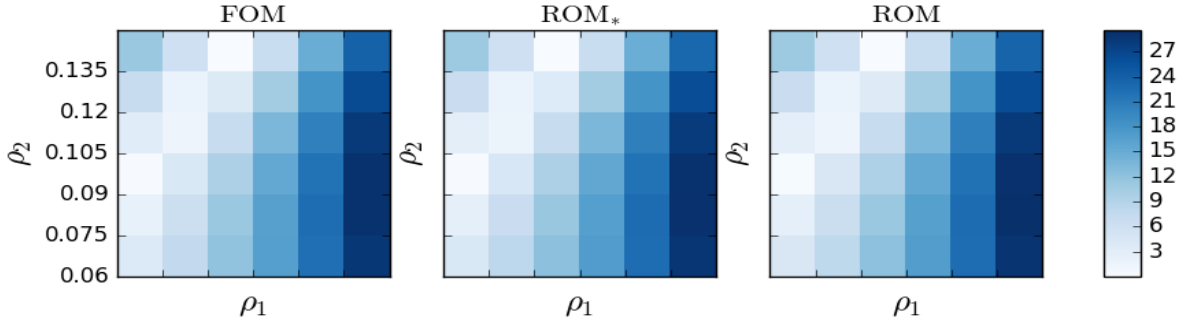

Fig. 28: $\dfrac{T_{22} - T_{11}}{T_{11}}$ obtained with FOM, ROM$_\star$ and ROM models.

5 Conclusion and perspectives

In this work, we proposed a POD-based model order reduction technique for efficient computation of the homogenized diffusion properties of periodic elementary cells parametrized by their geometries, for which classical model order reduction methods based on the computation of a spatial basis can not apply. This difficulty was overcome by the introduction of a transformation from a reference domain to the physical domain that is specially tailored to address the circular geometries used to model the microstructure in the framework of periodic homogenization of porous media. This transformation admits for three-dimensional geometries an explicit and exact affine decomposition that allows to split the problem into an offline learning phase and an online evaluation phase, so that the computational complexity of the latter does not depend on the number of degrees of freedom of the original full order solution space. We also provided an approximate yet accurate decomposition for two-dimensional geometries. The efficiency of the proposed POD-ROMs in terms of accuracy and computing time was shown for two dimensional and three dimensional isotropic or anisotropic elementary cells parametrized by a single parameter, and for elementary cells with multiple inclusions parametrized by several geometry parameters. For all the studied cases, the proposed POD-ROMs predict the homogenized diffusion properties with a relative error of the order of 10% compared with the value obtained by the Finite Element Method, and of the order of 1% in most cases, while dividing by 100 the computing time for two dimensional cells, and by $10s000$ for three dimensional cells. Two methods to compute the snapshots required to build the POD basis have been tested. The first one consists in solving the cell problem on the physical domain and transporting the solution to the reference domain. The second one is based on the resolution of the cell problem defined over the reference domain. Both methods give similar results, but the implementation of the first method is not intrusive and can be easily used with a classical FEM solver. Direct perspectives are the optimization-based parametric study of the microstructure from measured diffusion properties on real materials which would require repeated evaluation of the physical model for several different geometries, and the consideration of the nonlinearized Nernst-Plank-Poisson-Boltzmann equations.

Conflict of interest

The authors declare that they have no conflict of interest.

Acknowledgement

The authors would like to express their sincere thanks to the NEEDS program for having supported this work.

A Recalls on the Proper Orthogonal Decomposition (POD)

Reduced-order models consist in approximating the solution $\boldsymbol{\chi}_\star(\boldsymbol{\xi};\rho)$ of a given problem parametrized by ρ on a spatial basis $(\boldsymbol{\phi}_i)_{i=1}^{N_{\text{rom}}}$ of small size N_{rom}:

$$\boldsymbol{\chi}_\star(\boldsymbol{\xi};\rho) \simeq \widehat{\boldsymbol{\chi}}_\star(\boldsymbol{\xi};\rho) = \sum_{i=1}^{n_{\boldsymbol{\chi}}} a_i(\rho)\,\boldsymbol{\phi}_i(\boldsymbol{\xi})$$

where $\boldsymbol{\xi}$ is the space variable. There exists numerous methods to build this spatial basis, but the most used stays the Proper Orthogonal Decomposition that combines accuracy and optimality. The space-dependent functions $\boldsymbol{\phi}_i$ obtained by the POD, lying in the Hilbert space $\left(V_\star\right)^d$, satisfy the two conditions:

i) Orthogonality: $(\boldsymbol{\phi}_i)_i$ is orthogonal,

ii) Optimality of $(\boldsymbol{\phi}_i)_i$: $\boldsymbol{\phi}_l = \underset{\boldsymbol{\phi}\in\left(V_\star\right)^d}{\text{argmax}} \left\langle \left(\boldsymbol{\phi} \middle| \sum_{k=1}^{l-1} (\boldsymbol{\chi}_\star|\boldsymbol{\phi}_k)_{\left(V_\star\right)^d} \boldsymbol{\phi}_k \right)_{\left(V_\star\right)^d} \right\rangle,$

where $(\bullet|\bullet)_{\left(V_\star\right)^d}$ denotes the scalar product of $\left(V_\star\right)^d$ and $\langle\bullet\rangle$ denotes the mean over the variable ρ. The latter condition ensures that the space engendered by the $\{\boldsymbol{\phi}_i\}_{i=1}^l$ gives the best approximation of the functions $\boldsymbol{\chi}_\star(\boldsymbol{\xi};\rho)$, among the subspaces of $\left(V_\star\right)^d$ with rank l.

The method of snapshots introduced in [33] is used in this article. It consists in computing by the FEM a set of vector fields $\boldsymbol{\chi}_\star(\boldsymbol{\xi};\rho^j)$ (called the the snapshots) for a finite set of parameter values $\{\rho^j\}_{j=1}^{N_{\text{snap}}}$. Then, POD modes $\boldsymbol{\phi}_i$ are sought inside the functional space $[\boldsymbol{\chi}_\star(\boldsymbol{\xi};\rho^j)]_{j=1}^{N_{\text{snap}}}$. The snapshots $\boldsymbol{\chi}_\star(\boldsymbol{\xi};\rho^j)$ are expected to be linearly independent in practical cases so that, by exploiting the orthogonality and optimality conditions, the POD modes can be determined by the formula:

$$\boldsymbol{\phi}_i = \frac{1}{\sqrt{\lambda_i}} \sum_{j=1}^{N_{\text{snap}}} [\boldsymbol{v}_i]_j \boldsymbol{\chi}_\star(\boldsymbol{\xi};\rho^j),$$

where λ_i are the eigenvalues and $\boldsymbol{v}_i$ are the unit eigenvectors of the symmetric positive definite correlation matrix $\boldsymbol{C}$ whose coefficients are given by:

$$\boldsymbol{C}_{jk} = \frac{1}{N_{\text{snap}}} \int_\Omega \boldsymbol{\chi}_\star(\boldsymbol{\xi};\rho^k)\cdot\boldsymbol{\chi}_\star(\boldsymbol{\xi};\rho^j)\mathrm{d}\mathbf{y}.$$

The POD basis is then truncated to a number of $N_{\rm rom}$ modes which is selected to ensure that the error on the relative content of information due to the projection on the retained POD modes is below a given threshold ν:

$$N_{\rm rom} = \min \left\{ N \in 1 \dots N_{\rm snap};\ \frac{\sum_{i=1}^{N} \lambda_i}{\sum_{i=1}^{N_{\rm snap}} \lambda_i} > 1 - \nu \right\}. \tag{69}$$

B Formulas and proofs associated with the parametrized transformation

Let us recall the definition of transformation $\boldsymbol{\tau}_\rho$, for each $\boldsymbol{\xi}$ in the reference fluid domain:

$$\boldsymbol{\tau}_\rho(\boldsymbol{\xi}) = \begin{cases} \alpha_\rho \boldsymbol{u}(\boldsymbol{\xi}) + \beta_\rho \boldsymbol{\xi}, & \text{if } \rho_\star \leq \| \boldsymbol{\xi} \| < q, \\ \boldsymbol{\xi}, & \text{if } q \leq \| \boldsymbol{\xi} \|, \end{cases}$$

where $\rho_\star$ and q are the internal and external radii of the crown $\Omega_{\rm c}^\star$, $\boldsymbol{u}(\boldsymbol{\xi}) = \dfrac{\boldsymbol{\xi}}{\| \boldsymbol{\xi} \|}$ denotes the radial unit vector and

$$\alpha_\rho = q\frac{\rho - \rho_\star}{q - \rho_\star}, \quad \beta_\rho = \frac{q - \rho}{q - \rho_\star}.$$

The following formulas related with the Jacobian matrix of the transformation $\boldsymbol{\tau}_\rho$ are the core of the affine dependence to the geometry of the proposed POD-ROM.

Lemma 1 *For all ρ such that $\rho < q$:*

$$\boldsymbol{J}_\rho(\boldsymbol{\xi}) = \beta_\rho \boldsymbol{I} + \alpha_\rho \nabla_{\boldsymbol{\xi}} \boldsymbol{u}(\boldsymbol{\xi}), \tag{70}$$

$$\boldsymbol{J}_\rho^{-1}(\boldsymbol{\xi}) = \frac{1}{\beta_\rho}\boldsymbol{I} - \frac{\alpha_\rho}{\beta_\rho} \cdot \frac{1}{\beta_\rho \|\boldsymbol{\xi}\| + \alpha_\rho} \boldsymbol{G}_{\boldsymbol{u}(\boldsymbol{\xi})}, \tag{71}$$

$$j_\rho(\boldsymbol{\xi}) = \beta_\rho \sum_{p=0}^{d-1} C_{d-1}^p \frac{\alpha_\rho^p}{\|\boldsymbol{\xi}\|^p} \beta_\rho^{d-1-p}, \tag{72}$$

with the convention :

$$\boldsymbol{G}_{\boldsymbol{u}(\boldsymbol{\xi})} \colon = \boldsymbol{I} - \frac{1}{\|\boldsymbol{\xi}\|^2} \boldsymbol{\xi} \cdot \boldsymbol{\xi}^{\mathsf{T}}. \tag{73}$$

Proof (70) is obvious, it follows from the definition of $\boldsymbol{\tau}_\rho$ and the linearity of the gradient operator. To prove (71) we need an explicit formula for the inverse mapping ${\boldsymbol{\tau}_\rho}^{-1}$. We firstly notice that, according to the geometrical characterization of $\boldsymbol{\tau}_\rho$ at the beginning of section 3, ${\boldsymbol{\tau}_\rho}^{-1}$ is obtained by switching $\rho_\star$ and ρ in $\boldsymbol{\tau}_\rho$. Then we have for $\boldsymbol{y} = \boldsymbol{\tau}_\rho(\boldsymbol{\xi})$:

$${\boldsymbol{\tau}_\rho}^{-1}(\boldsymbol{y}) = \begin{cases} \alpha'_\rho \boldsymbol{u}(\boldsymbol{y}) + \beta'_\rho \boldsymbol{y}, & \text{if } \rho_\star \leq \| \boldsymbol{y} \| < q, \\ \boldsymbol{y}, & \text{if } q \leq \| \boldsymbol{y} \|, \end{cases}$$

where

$$\alpha'_\rho = q\frac{\rho_\star - \rho}{q - \rho}, \quad \beta'_\rho = \frac{q - \rho_\star}{q - \rho}.$$

Note that $\alpha'_\rho = -\frac{\alpha_\rho}{\beta_\rho}$ and $\beta'_\rho = \frac{1}{\beta_\rho}$. Now, differentiating ${\boldsymbol{\tau}_\rho}^{-1}$ at $\boldsymbol{\tau}_\rho(\boldsymbol{\xi})$ to compute $\boldsymbol{J}_\rho^{-1}(\boldsymbol{\xi})$ for each $\boldsymbol{\xi} < q$ yields $\boldsymbol{J}_\rho^{-1}(\boldsymbol{\xi}) = \left(\nabla_{\boldsymbol{\tau}_\rho(\boldsymbol{\xi})} {\boldsymbol{\tau}_\rho}^{-1}\right)(\boldsymbol{\tau}_\rho(\boldsymbol{\xi}))$, from which it follows by linearity that

$$\boldsymbol{J}_\rho^{-1}(\boldsymbol{\xi}) = \frac{1}{\beta_\rho}\left(\boldsymbol{I} - \alpha_\rho \nabla_{\boldsymbol{\tau}_\rho(\boldsymbol{\xi})} \boldsymbol{u}(\boldsymbol{\tau}_\rho(\boldsymbol{\xi}))\right).$$

By definition of the unitary vector $\boldsymbol{u}(\boldsymbol{y}) = \dfrac{\boldsymbol{y}}{\|\boldsymbol{y}\|}$, we have $\nabla_{\boldsymbol{y}} \boldsymbol{u}(\boldsymbol{y}) = \frac{1}{\|\boldsymbol{y}\|}\left(\boldsymbol{I} - \frac{1}{\|\boldsymbol{y}\|^2}\boldsymbol{y} \cdot \boldsymbol{y}^{\mathsf{T}}\right)$. To conclude, notice that $\boldsymbol{G}_{\boldsymbol{u}(\boldsymbol{\xi})} = \boldsymbol{G}_{\boldsymbol{u}(\boldsymbol{y})}$ since $\boldsymbol{\tau}_\rho(\boldsymbol{\xi})$ is always positively co-linear to $\boldsymbol{\xi}$ so that

$$\boldsymbol{J}_\rho^{-1}(\boldsymbol{\xi}) = \frac{1}{\beta_\rho}\left(\boldsymbol{I} - \alpha_\rho \frac{1}{\|\boldsymbol{\tau}_\rho(\boldsymbol{\xi})\|}\left(\boldsymbol{I} - \frac{1}{\|\boldsymbol{\xi}\|^2}\boldsymbol{\xi} \cdot \boldsymbol{\xi}^{\mathsf{T}}\right)\right),$$

which provides the expected result.
Thereafter, we provide the proof of the latest statement (72) in the case $d = 3$. Notice that the matrix $\boldsymbol{\xi} \cdot \boldsymbol{\xi}^{\mathsf{T}}$ is by construction of rank 1 and symmetric so that it exists an orthogonal matrix $\boldsymbol{P}$ for which

$$\boldsymbol{\xi} \cdot \boldsymbol{\xi}^{\mathsf{T}} = \boldsymbol{P} \cdot \begin{pmatrix} \mathrm{Tr}\ (\boldsymbol{\xi} \cdot \boldsymbol{\xi}^{\mathsf{T}}) & 0 & 0 \\ 0 & 0 & 0 \\ 0 & 0 & 0 \end{pmatrix} \cdot \boldsymbol{P}^{\mathsf{T}}.$$

Moreover, we have $\mathrm{Tr}(\boldsymbol{\xi} \cdot \boldsymbol{\xi}^{\mathsf{T}}) = \|\boldsymbol{\xi}\|^2$ for all $\boldsymbol{\xi}$ so that

$$\nabla_{\boldsymbol{\xi}} \boldsymbol{u}(\boldsymbol{\xi}) = \boldsymbol{P} \cdot \begin{pmatrix} 0 & 0 & 0 \\ 0 & \frac{1}{\|\boldsymbol{\xi}\|} & 0 \\ 0 & 0 & \frac{1}{\|\boldsymbol{\xi}\|} \end{pmatrix} \cdot \boldsymbol{P}^{\mathsf{T}},$$

and

$$\boldsymbol{J}_\rho(\boldsymbol{\xi}) = \boldsymbol{P} \cdot \begin{pmatrix} \beta_\rho & 0 & 0 \\ 0 & \beta_\rho + \frac{\alpha_\rho}{\|\boldsymbol{\xi}\|} & 0 \\ 0 & 0 & \beta_\rho + \frac{\alpha_\rho}{\|\boldsymbol{\xi}\|} \end{pmatrix} \cdot \boldsymbol{P}^{\mathsf{T}}.$$

We deduce the formula (72) by expending the expression $\beta_\rho\left(\beta_\rho + \frac{\alpha_\rho}{\|\boldsymbol{\xi}\|}\right)^{d-1}$ using the binomial theorem. □

Notice that this demonstration relies on the symmetry of $\boldsymbol{J}_\rho(\boldsymbol{\xi})$ which stands from the spherical symmetry of the transformation $\boldsymbol{\tau}_\rho$, so that it does not generalize directly to other kind of transformations. We are ready to establish the two main statements of this paragraph.

Theorem 1

$$\boldsymbol{J}_\rho^{-1}\, j_\rho = \begin{cases} \left(\beta_\rho + \alpha_\rho \frac{1}{\|\boldsymbol{\xi}\|}\right)\boldsymbol{I} - \alpha_\rho \frac{1}{\|\boldsymbol{\xi}\|}\boldsymbol{G}_{\boldsymbol{u}(\boldsymbol{\xi})}, & \text{if } d=2\,, \\ \left(\beta_\rho^2 + 2\alpha_\rho\beta_\rho \frac{1}{\|\boldsymbol{\xi}\|} + \alpha_\rho^2 \frac{1}{\|\boldsymbol{\xi}\|^2}\right)\boldsymbol{I} - \alpha_\rho\left(\beta_\rho \frac{1}{\|\boldsymbol{\xi}\|} + \alpha_\rho \frac{1}{\|\boldsymbol{\xi}\|^2}\right)\boldsymbol{G}_{\boldsymbol{u}(\boldsymbol{\xi})}, & \text{if } d=3\,. \end{cases}$$

Proof From lemma 1 and the following equality

$$j_\rho = \beta_\rho \left(\frac{\|\boldsymbol{\tau}_\rho(\boldsymbol{\xi})\|}{\|\boldsymbol{\xi}\|}\right)^{d-1},$$

we have

$$\boldsymbol{J}_\rho^{-1}\, j_\rho = \beta_\rho \left(\frac{\|\boldsymbol{\tau}_\rho(\boldsymbol{\xi})\|}{\|\boldsymbol{\xi}\|}\right)^{d-1} \left(\frac{1}{\beta_\rho}\boldsymbol{I} - \frac{\alpha_\rho}{\beta_\rho}\cdot\frac{1}{\beta_\rho\|\boldsymbol{\xi}\| + \alpha_\rho}\boldsymbol{G}_{\boldsymbol{u}(\boldsymbol{\xi})}\right).$$

The multiplication by $\|\boldsymbol{\tau}_\rho(\boldsymbol{\xi})\|^{d-1}$ simplifies the denominator which is due to $\boldsymbol{J}_\rho^{-1}$, whatever d can be. This yields the expected formulas. □

Theorem 2

$$\boldsymbol{J}_\rho^{-2}\, j_\rho = \begin{cases} \left(1 + \frac{\alpha_\rho}{\beta_\rho\|\boldsymbol{\xi}\|}\right)\boldsymbol{I} - \left(1 + \beta_\rho^{n_\mathrm{t}+1} + (1-\beta_\rho)\left(\sum_{l=1}^{n_\mathrm{t}}(-1)^l\left(\sum_{m=l}^{n_\mathrm{t}}\beta_\rho^m C_m^l\right)\frac{\|\boldsymbol{\xi}\|^l}{q^l} + \mathcal{R}_{n_\mathrm{t}}(\rho,\boldsymbol{\xi})\right)\right)\frac{\alpha_\rho}{\beta_\rho\|\boldsymbol{\xi}\|}\boldsymbol{G}_{\boldsymbol{u}(\boldsymbol{\xi})} & \text{if } d=2\,, \\ \left(\beta_\rho + 2\alpha_\rho\frac{1}{\|\boldsymbol{\xi}\|} + \frac{\alpha_\rho^2}{\beta_\rho}\frac{1}{\|\boldsymbol{\xi}\|^2}\right)\boldsymbol{I} - 2\alpha_\rho\frac{1}{\|\boldsymbol{\xi}\|}\boldsymbol{G}_{\boldsymbol{u}(\boldsymbol{\xi})} - \frac{\alpha_\rho^2}{\beta_\rho}\frac{1}{\|\boldsymbol{\xi}\|^2}\boldsymbol{G}_{\boldsymbol{u}(\boldsymbol{\xi})}, & \text{if } d=3\,, \end{cases}$$

where the residual is given by $\mathcal{R}_{n_\mathrm{t}}(\rho,\boldsymbol{\xi}) = \left(\frac{\beta_\rho}{q}(q-\|\boldsymbol{\xi}\|)\right)^{n_\mathrm{t}+1}\frac{1}{1-\beta_\rho\frac{q-\|\boldsymbol{\xi}\|}{q}}$.

Proof As well as in the proof of theorem 1 we have

$$\left(\boldsymbol{J}_\rho^{-2}\right) j_\rho = \beta_\rho\left(\frac{\|\boldsymbol{\tau}_\rho(\boldsymbol{\xi})\|}{\|\boldsymbol{\xi}\|}\right)^{d-1}\left(\frac{1}{\beta_\rho}\boldsymbol{I} - \frac{\alpha_\rho}{\beta_\rho}\left(\frac{1}{\beta_\rho\|\boldsymbol{\xi}\| + \alpha_\rho}\boldsymbol{G}_{\boldsymbol{u}(\boldsymbol{\xi})}\right)\right)^2 \tag{74}$$

ù The result announced for $d=3$ follows easily, but the same reasoning fails when $d=2$: indeed, the multiplication by $\|\boldsymbol{\tau}_\rho(\boldsymbol{\xi})\| = \alpha_\rho + \beta_\rho\|\boldsymbol{\xi}\|$ does not compensate the presence of $\left(\frac{1}{\beta_\rho\|\boldsymbol{\xi}\| + \alpha_\rho}\right)^2$ in the latest expression. Unfortunately, the fraction $\frac{1}{\beta_\rho\|\boldsymbol{\xi}\| + \alpha_\rho}$ is an obstruction for the offline computation required for the algorithms 1–2. We overcome this difficulty by approximating $\left(\boldsymbol{J}_\rho^{-2}\right) j_\rho$: starting from (74) we get:

$$\left(\boldsymbol{J}_\rho^{-2}\right) j_\rho = \boldsymbol{I} + \frac{\alpha_\rho}{\beta_\rho\|\boldsymbol{\xi}\|}\boldsymbol{I} - 2\frac{\alpha_\rho}{\beta_\rho\|\boldsymbol{\xi}\|}\boldsymbol{G}_{\boldsymbol{u}(\boldsymbol{\xi})} + \frac{\alpha_\rho}{\beta_\rho\|\boldsymbol{\xi}\|}(1-\beta_\rho)\cdot\frac{1}{1-\beta_\rho\frac{q-\|\boldsymbol{\xi}\|}{q}}\boldsymbol{G}_{\boldsymbol{u}(\boldsymbol{\xi})} \tag{75}$$

The key point is the following, intermediate result:

Lemma 2 *For every* ρ *and* $\rho_\star \leq \|\boldsymbol{\xi}\| < q$, *we have*

$$\beta_\rho\frac{q-\|\boldsymbol{\xi}\|}{q} \in \left[0, \frac{q-\rho}{q}\right]. \tag{76}$$

Consequently and for all $0<\rho<q$, *this ratio belongs to* $]0,1[$.

Then the fraction $\frac{1}{1-\beta_\rho\frac{q-\|\boldsymbol{\xi}\|}{q}}$ can be developped as a power series, which entails:

$$\left(\boldsymbol{J}_\rho^{-2}\right) j_\rho = \left(1 + \frac{\alpha_\rho}{\beta_\rho\|\boldsymbol{\xi}\|}\right)\boldsymbol{I} - 2\frac{\alpha_\rho}{\beta_\rho\|\boldsymbol{\xi}\|}\boldsymbol{G}_{\boldsymbol{u}(\boldsymbol{\xi})} + \left(\sum_{m=0}^{n_\mathrm{t}}\left(\frac{\beta_\rho}{q}\right)^m\cdot(q-\|\boldsymbol{\xi}\|)^m\right)(1-\beta_\rho)\frac{\alpha_\rho}{\beta_\rho\|\boldsymbol{\xi}\|}\cdot\boldsymbol{G}_{\boldsymbol{u}(\boldsymbol{\xi})} + \mathcal{R}_{n_\mathrm{t}}(\rho,\boldsymbol{\xi})(1-\beta_\rho)\frac{\alpha_\rho}{\beta_\rho\|\boldsymbol{\xi}\|}\cdot\boldsymbol{G}_{\boldsymbol{u}(\boldsymbol{\xi})}. \tag{77}$$

where $\mathcal{R}_{n_\mathrm{t}}(\rho,\boldsymbol{\xi})$ is the announced residual of order n_t. The latter vanishes when $n_\mathrm{t}\to+\infty$ according to lemma 2, and in practical cases the convergence is very fast (we use $n_\mathrm{t}\leq 3$ for all numerical applications in this work). To fully establish the affine separation of $\boldsymbol{\xi}$ and ρ we write:

$$\sum_{m=0}^{n_\mathrm{t}}\left(\frac{\beta_\rho}{q}\right)^m\cdot(q-\|\boldsymbol{\xi}\|)^m = \sum_{m=0}^{n_\mathrm{t}}\beta_\rho^m\left(1-\frac{\|\boldsymbol{\xi}\|}{q}\right)^m = \sum_{m=0}^{n_\mathrm{t}}\sum_{l=0}^{m}\beta_\rho^m\, C_m^l(-1)^l\frac{\|\boldsymbol{\xi}\|^l}{q^l} = \sum_{l=0}^{n_\mathrm{t}}\sum_{m=l}^{n_\mathrm{t}}\beta_\rho^m\, C_m^l(-1)^l\frac{\|\boldsymbol{\xi}\|^l}{q^l}. \tag{78}$$

For $l=0$, the sum $\sum_{m=l}^{n_\mathrm{t}}\beta_\rho^m\, C_m^l(-1)^l\frac{\|\boldsymbol{\xi}\|^l}{q^l}$ is a geometric sum and equals $\frac{1-\beta_\rho^{n_\mathrm{t}+1}}{1-\beta_\rho}$, so that

$$-2\frac{\alpha_\rho}{\beta_\rho\|\boldsymbol{\xi}\|}\boldsymbol{G}_{\boldsymbol{u}(\boldsymbol{\xi})} + \sum_{m=l}^{n_\mathrm{t}}\beta_\rho^m\, C_m^l(-1)^l\frac{\|\boldsymbol{\xi}\|^l}{q^l}(1-\beta_\rho)\frac{\alpha_\rho}{\beta_\rho\|\boldsymbol{\xi}\|}\boldsymbol{G}_{\boldsymbol{u}(\boldsymbol{\xi})} = -(1+\beta_\rho^{1+n_\mathrm{t}})\frac{\alpha_\rho}{\beta_\rho\|\boldsymbol{\xi}\|}\boldsymbol{G}_{\boldsymbol{u}(\boldsymbol{\xi})} \text{ for } l=0. \tag{79}$$

Injecting (78) and (79) into (77) gives the announced statement. Provided a rank n_t for which the residual $\mathcal{R}_{n_\mathrm{t}}(\rho,\boldsymbol{\xi})$ can be neglected, we obtain an expression of $\left(\boldsymbol{J}_\rho^{-2}\right) j_\rho$ where variables ρ and $\boldsymbol{\xi}$ are separated. □

Notice that since the inequality stated in lemma 2 is normalized by q, the same n_t can be chosen for each inclusion in the multiparametric case, indifferently to the size of the inclusions. It is the case for hte numerical applications of this work, although a unique q has been used in this work.

References

1. Abdulle A. ans Bai, Y.: Reduced-order modelling numerical homogenization. Philosophical transactions of the Royal Society **372** (2013)
2. Allaire, G.: Homogenization and two-scale convergence. Journal of Mathematical Analysis and Applications **23**, 1482–1518 (1992)
3. Allery, C., Beghein, C., Hamdouni, A.: On investigation of Particle dispersion by a POD approach. International Applied Mechanics **44**(1), 110–119 (2008). DOI 10.1007/s10778-008-0025-2
4. Auriault, J.L., Boutin, C., Geindreau, C.: Homogenization of Coupled Phenomena in Heterogenous Media. Wiley (2009)
5. Auriault, J.L., Lewandowska, J.: Diffusion/adsorption/advection macrotransport in soils. European Journal of Mechanics **15**, 681–704 (1996)
6. Bansoussan, A., Lions, J.L., Papanicolaou, G.: Asymptotic Analysis fir Periodic Structures. AMS chelsea publishing (1978)
7. Bergmann, M., Cordier, L.: Optimal control of the cylinder wake in the laminar regime by trust-region methods and POD reduced-order models. Journal of Computational Physics **227**(16), 7813–7840 (2008). DOI 10.1016/j.jcp.2008.04.034
8. Bourbatache, K., Millet, O., Aït-Mokhtar, A.: Ionic transfer with electrocapillary interactions in cementitious porous media. periodic homogenization and parametric study on 2d micro-structures. International Journal of Heat and Mass Transfer **55**, 5979–5991 (2012)
9. Bourbatache, K., Millet, O., Aït-Mokhtar, A., Amiri, O.: Modeling chlorides transport in cementitious materials using periodic homogenization. Transport in Porous Media **94**(1), 437–459 (2012)
10. Bourbatache, K., Millet, O., Aït-Mokhtar, A., Amiri, O.: Chloride transfer in cement-based materials. Part 1. theoretical basis and modelling. International Journal For Numerical And Analytical Methods In Geomechanics **37**, 1614–1627 (2013)
11. Bourbatache, K., Millet, O., Aït-Mokhtar, A., Amiri, O.: Chloride transfer in cement-based materials. Part 2. experimental study and numerical simulations. International Journal For Numerical And Analytical Methods In Geomechanics **37**, 1628–1641 (2013)
12. Bourbatache, K., Millet, O., Moyne, C.: Upscaling diffusion-reaction in porous media. Acta Mechanica **231**(2) (2020)
13. Bourbatache, M.K., Bennai, F., Zhao, C., Millet, O., Aït-Mokhtar, A.: Determination of geometrical parameters of the microstructure of a porous medium: application to cementitious materials. International Communications in Heat and Mass Transfer **117** (2020)
14. Bourbatache, M.K., Millet, O., Aït-Mokhtar, A.: Ionic transfer in charged porous media. International journal of Heat and Mass Transfer **55**, 5979–5991 (2012)
15. Bourbatache, M.K., Millet, O., Aït-Mokhtar, A.: Multiscale periodic homogenization if ionic transfer in cementitious materials. International journal of Heat and Mass Transfer **52**, 1489–1499 (2016)
16. Brigham, J.C., Aquino, W.: Inverse viscoelastic material characterization using pod reduced-order modeling in acoustic-structure interaction. Computational Methods Appl. Mech. Engrg. **198**, 893–903 (2009)
17. Ekre, F., Larsson, F., Runesson, K., Jänicke, R.: A posteriori error estimation for numerical model reduction in computational homogenization of porous media. International Journal for Nuerical Methods in Engineering **121**, 5350, 5380 (2020)
18. Gagneux, G., Millet, O.: General properties of the Nernst-Planck-Poisson-Boltzmann system describing electrocapillary effects in porous media. Journal of Elasticity **117**, 213–230 (2014)
19. Gagneux, G., Millet, O.: Homogenization of the Nernst-Planck-Poisson system by two-scale convergence. Journal of Elasticity **114**, 69–84 (2014)
20. Gagneux, G., Millet, O.: A survey on properties of Nernst-Planck-Poisson system. application to cementitious materials. Applied Mathematical Modelling **40**, 846–858 (2016)
21. Hornung, U.: Diffusion, convection, adsorption, and reaction of chemicals in porous media. Journal of Differential Equations **92**, 199–225 (1991)
22. Hornung, U.: Homogenization of Porous Media. Springer (1997)
23. Jänicke, R.: Computational homogenization and reduced-order modeling of diffusion processes in fluid-saturated porous media. Ph.D. thesis, Institüt für Mechanik, Ruhr-Universität Bochum (2015)
24. Lumley, J.L.: The structure of inhomogeneous turbulence. Atmospheric Turbulence and Wave propagation pp. 166–178 (1967)
25. Mchirgui, W., Millet, O., Amiri, O., Belarbi, R.: Moisture transport in cementitious materials. periodic homogenization and numerical analysis. European Journal of Environmental and Civil Engineering **21**, 1026–1042 (2017)
26. Moyne, C., Murad, M.: A two-scale model for coupled electro-chemo-mechanical phenomena and onsager's reciprocity relations in expansive clays: I homogenization analysis. Transport in Porous Media **62**, 333–380 (2006)
27. Quarteroni, A., Manzoni, A., Negri, F.: Reduced Basis Methods for Partial Differential Equations: An introduction. Springer (2016)
28. Quintard, M., Whitaker, S.: Convection, dispersion, and interfacial transport of contaminants : Homogeneous porous media. Advances in Water Ressources **17**(4), 221–239 (1993)
29. Quintard, M., Whitaker, S.: Two-phase flow in heterogeneous porous media : The method of large-scale averaging. Transport in Porous Mewill bedia **3**, 357–413 (1993)
30. Rozza, G., Huynh, D.B., Patera, A.T.: Reduced basis approximation and a posteriori error estimation for affinely parametrized elliptic coercive Partial Differential Equations. Archives on Computational Methods in Engineering **15**(229) (2008)
31. Rozza, G., Huynh, D.B.P., Manzoni, A.: Reduced basis approximation and a posteriori error estimation for Stokes flows in parametrized geometries : roles of the inf-sup stability constants. Numerische Mathematik **125**, 115–152 (2013)
32. Sanchez-Palencia, E.: Non Homogeneous Media and Vibration Theory. Springer (1980)
33. Sirovich, L.: Turbulence and the dynamics of coherent structures. I. coherent structures. Quarterly of applied mathematics **45**(3), 561–571 (1987)
34. Stemelen D. abd Moyne, C., Lemaire, T.: Modelling of electro-osmosis in clayery materials including PH effects. Physics abd Chelistry of the Earth **31**, 441–452 (2007)
35. Tallet, A., Allery, C., Leblond, C., Liberge, E.: A minimum residual projection to build coupled velocity-pressure POD-ROM for incompressible navier-Stokes equations. Communications in Nonlinear Science and Numerical Simulation **22**(1-3), 909–932 (2015). DOI 10.1016/j.cnsns.2014.09.009
36. Yvonnet, J., He, Q.C.: The reduced model multiscale method (R3M) for the non-linear homogenization of hyperelastic media at finite strains. Journal of Computational Physics **223**(1), 341–368 (2007)
37. Yvonnet, J., Moneiro, E., He, Q.C.: Computational homogenization method and reduced database model for hyperelastic heterogeneous structures. International Journal for Nuerical Methods in Engineering **11**, 201–225 (2013)